DEPARTMENT OF ASTRONOMY

The University of Wisconsin-Madison
475 N Charter Street
Madison Wisconsin 53706-1582
Telephone: (608) 262-3071
FAX: (608) 263-6386
http://www.astro.wisc.edu

DOCUMENT IDENTIFICATION:

PROJECT:	**SOUTHERN AFRICAN LARGE TELESCOPE ROBERT STOBIE SPECTROGRAPH NEAR INFRARED INSTRUMENT**
DOCUMENT TITLE:	**THERMAL STRAY LIGHT ANALYSIS**
DOCUMENT #:	**SALT-3501AA0002**
FILENAME:	
REVISION:	-
KEYWORDS:	

APPROVALS:

AUTHOR:	Date: _____ Marsha Wolf Project Scientist
ENGINEERING:	Date: _____ Don Thielman System Engineer
QUALITY:	Date: _____ Tom Demke Quality Assurance
PROJECT:	Date: _____ Andrew Sheinis Principal Investigator

REVISION HISTORY:

Rev	ECN	Description	Date	Approval
Draft	NA	Original Document	7 May 2009	

Contents

1   Introduction

The near infrared arm of the Robert Stobie Spectrograph (RSS-NIR) on the Southern African Large Telescope (SALT) is a semi-warm instrument, working in a regime where a number of spectrographs have not been successful. Therefore, from the beginning, detailed thermal stray light analysis has been a high priority for the project, and is integral to the entire design. Our analysis is performed using the Advanced Systems Analysis Program (ASAP) by Breault Research Organization. The optical design of SALT, RSS, and the NIR arm are directly imported into ASAP from Zemax and the mechanical designs of mounts and structures are directly imported from SolidWorks. Every component can be made into a thermal emitter with the proper temperature, emissivity, and scattering characteristics. Initially, our model of the NIR arm in ASAP was largely conceptual, but allowed us to roughly determine required operating temperatures of regions of components early in the project. As the mechanical design of the instrument matures, the ASAP model will be used to design baffles, the cold pupil mask, and radiation shields within the cooled areas. Preliminary results of the instrument thermal backgrounds predicted from ASAP have already been incorporated into our instrument performance simulator.

Figure 1. RSS instrument layout. The common components are the slit, collimator, and dichroic beamsplitter. The visible beam is reflected by the dichroic and the components of that arm are shown as in gray on the right. The NIR beam is transmitted through the dichroic to its final doublet of the collimator. The NIR doublet also serves as the window into the pre-dewar enclosure (see **Figure 2**). The cryogenic dewar begins at the 6th NIR camera lens. Both instruments sit on the existing space frame that was constructed for RSS-VIS.

A brief overview of RSS-NIR is given in Section 2. Section 3 contains a description of the ambient temperature components that are common to both the visible and NIR instrument arms. We began the thermal analysis with the ambient temperature components for two reasons: 1) we expect them to be the largest contributors to the instrument thermal background, and 2) they already exist for the visible side of the instrument, so details of their thermal emission could be analyzed early in our NIR instrument design phases. Section 4 describes our initial estimates for the required operating temperature of a cooled pre-dewar section, using an early conceptual design of the pre-dewar. Further analysis of the details in this section will continue once the mechanical designs mature. Section 5 describes the parts of the telescope that are included in the thermal analysis. Thermal background results are presented in Section 6, including an analysis of SALT temperature data and translating them into amounts of time during the year that different observations will be possible. Section 7 discusses issues related to the long wavelength cutoff of the instrument, including detector quantum efficiency fall-off at long wavelengths and our preliminary selection of long wavelength blocking filters. Other semi-warm NIR spectrographs are contrasted in Section 8 and our initial conclusions leading to the baseline design for RSS-NIR are summarized in Section 9.

2   Instrument Overview

A model of the RSS system is shown in **Figure 1**. The beam comes up from the telescope below to a focus at the slit plane. The slit, waveplates, collimator, and dichroic beamsplitter form the common optical path. At the dichroic the visible beam splits off to the right and the NIR beam is transmitted up to a fold mirror which sends the light to the left.

RSS-NIR was originally conceived to have three different temperature environments, as depicted in **Figure 2**: cryogenic, below ambient, and ambient. A cryogenic dewar houses the detector, long wavelength blocking filters, and last 2 camera optics, one of which is the entrance window. A pre-dewar, cooled to approximately -40 °C, contains all components between the cryogenic dewar and the NIR collimator doublet. These components include the NIR doublet lenses (the first element is the window between the pre-dewar and the ambient observatory), the fold mirror, order sorting filters for Fabry-Perot mode, the Fabry-Perot etalon, the spectroscopic gratings, the polarizing beamsplitter, the first 5 camera optics, and mounts and actuators for all of these components. The final section is not cooled and floats at the ambient temperature. These are the common optics: the dichroic beamsplitter, the collimator optics, the waveplates, the field lens, and the slit mechanism.
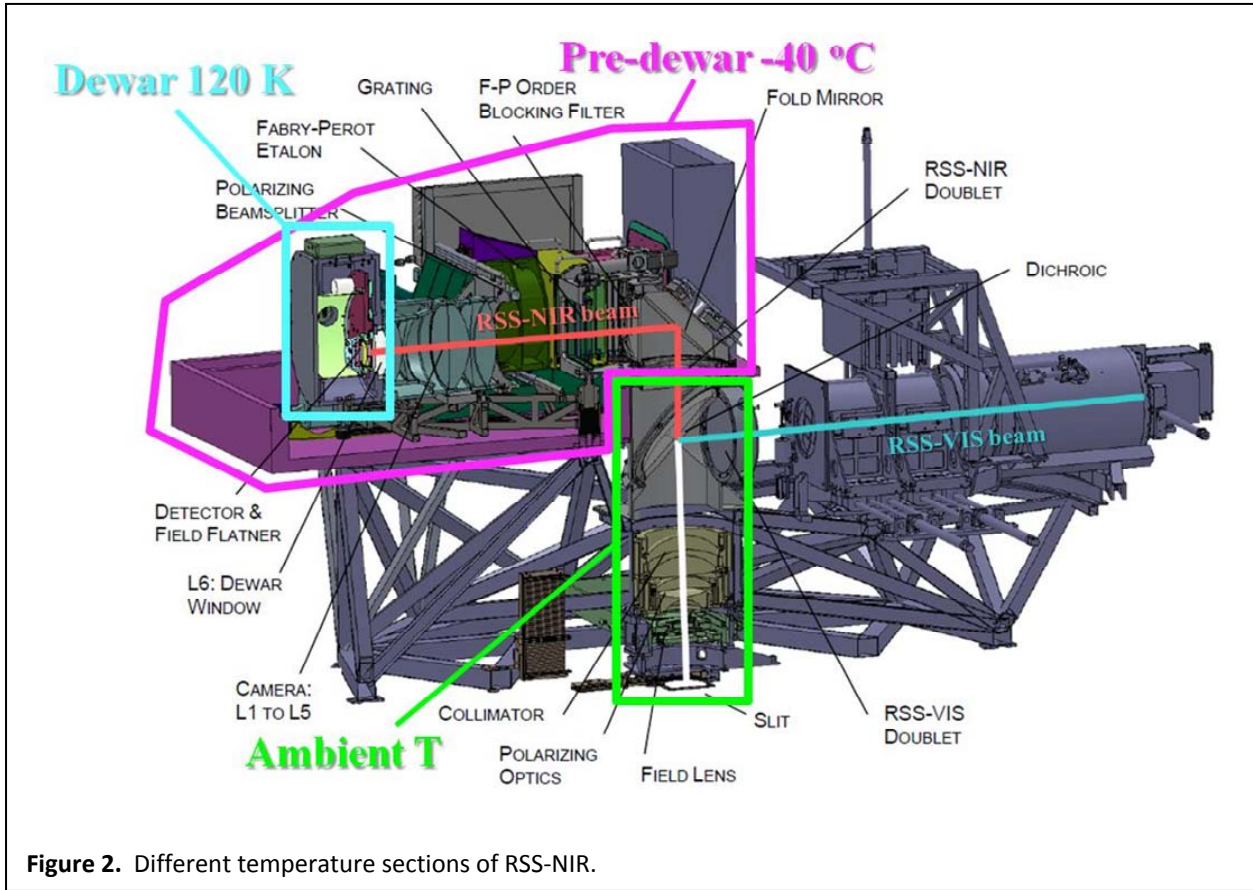
Figure 2. Different temperature sections of RSS-NIR.

3 Common Components

3.1 Slit Masks

3.1.1 Long slits

The slit plane is located at the bottom of the RSS, and is the first element with which photons interact in the instrument. It is common to both the visible and NIR arms of RSS. We refer to the first side that photons see as the bottom and the side facing the detector as the top. The long slits, shown in **Figure 3**, consist of a stainless steel slit blank that is assembled in its mount at an 11° angle so that the SALTICAM slit viewing camera has access to the bottom side. The blank has a 1 arcsec wide slit cut into it. The surfaces that are set up to be thermal emitters in the analysis are listed in **Table 1**. All surfaces are assumed to be gold coated with ε=0.02. Only top surfaces facing the detector are analyzed.
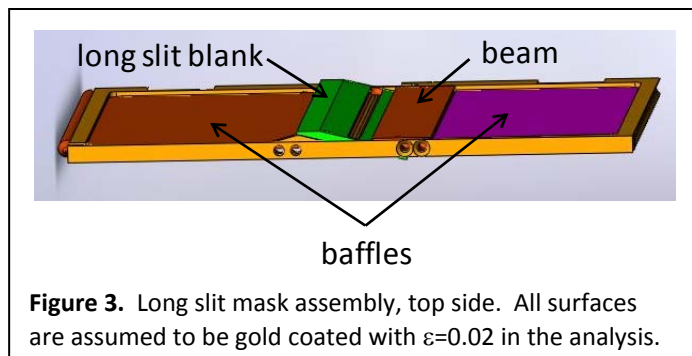

Figure 3. Long slit mask assembly, top side. All surfaces are assumed to be gold coated with ε=0.02 in the analysis.

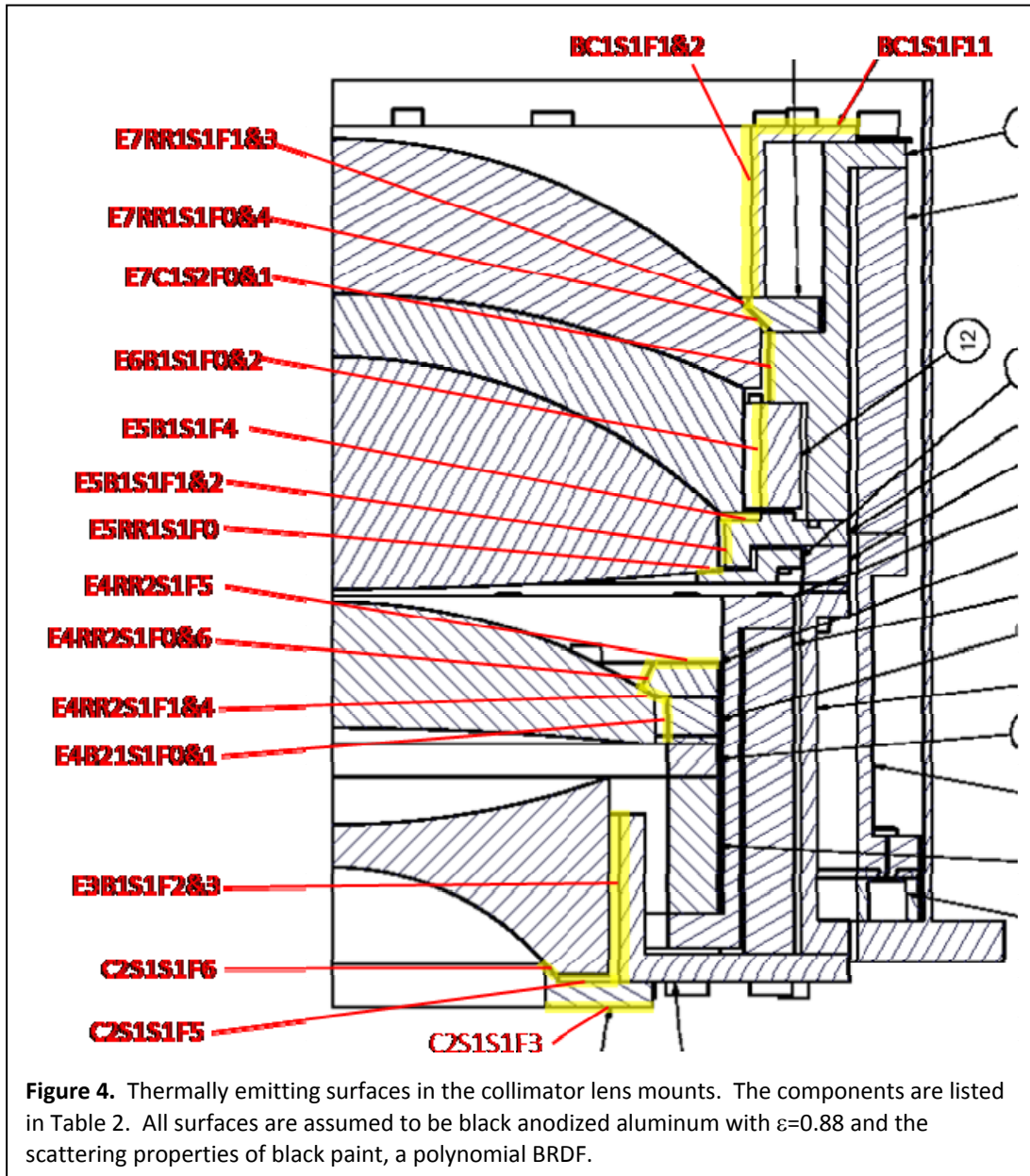**Table 1.** Thermally emitting surfaces in the long slit assembly.

Source	Component
1	flat portion of long slit blank
2	top surface of slit blank
3	1st indentation toward slit
4	inner indentation for slit
5	long slit beam
6	baffle
7	baffle

Table 2. Thermally emitting surfaces in the collimator lens mounts.

Source	Label	Component
1	BC1S1F11	BLADDER_COVER_1_surface1_Face11
2	BC1S1F1	BLADDER_COVER_1_surface1_Face1
3	BC1S1F2	BLADDER_COVER_1_surface1_Face2
4	E7RR1S1F0	ELEMENT_7_RETAINING_RING_1_surface1_Face0
5	E7RR1S1F4	ELEMENT_7_RETAINING_RING_1_surface1_Face4
6	E7RR1S1F1	ELEMENT_7_RETAINING_RING_1_surface1_Face1
7	E7RR1S1F3	ELEMENT_7_RETAINING_RING_1_surface1_Face3
8	E7C1S2F0	ELEMENT_7_CELL_1_surface2_Face0
9	E7C1S2F1	ELEMENT_7_CELL_1_surface2_Face1
10	E6B1S1F0	ELEMENT_6_BEZEL_1_surface1_Face0
11	E6B1S1F2	ELEMENT_6_BEZEL_1_surface1_Face2
12	E5B1S1F4	ELEMENT_5_BEZEL_1_surface1_Face4
13	E5B1S1F1	ELEMENT_5_BEZEL_1_surface1_Face1
14	E5B1S1F2	ELEMENT_5_BEZEL_1_surface1_Face2
15	E5RR1S1F0	ELEMENT_5_RETAINING_RING_1_surface1_Face0
16	E4RR21S1F5	ELEMENT_4_RETAINING_RING_2_1_surface1_Face5
17	E4RR21S1F1	ELEMENT_4_RETAINING_RING_2_1_surface1_Face1
18	E4RR21S1F4	ELEMENT_4_RETAINING_RING_2_1_surface1_Face4
19	E4RR21S1F6	ELEMENT_4_RETAINING_RING_2_1_surface1_Face6
20	E4RR21S1F0	ELEMENT_4_RETAINING_RING_2_1_surface1_Face0
21	E4B21S1F0	ELEMENT_4_BEZEL_2_1_surface1_Face0
22	E4B21S1F1	ELEMENT_4_BEZEL_2_1_surface1_Face1
23	E3B1S1F2	ELEMENT_3_BEZEL_1_surface1_Face2
24	E3B1S1F3	ELEMENT_3_BEZEL_1_surface1_Face3
25	C2S1S1F5	CELL_2_SEAT_1_surface1_Face5
26	C2S1S1F6	CELL_2_SEAT_1_surface1_Face6
27	C2S1S1F3	CELL_2_SEAT_1_surface1_Face3

3.2 Collimator Mounts

The mounts for the common RSS optics are black anodized aluminum, assuming ε=0.88. All surfaces that face lens surfaces, retaining rings and cell walls, or that face toward the detector or slit, top and bottom horizontal rings, are set up as thermal emitters. These surfaces for the collimator mounts are shown in **Figure 4** and listed in **Table 2**.

Figure 4. Thermally emitting surfaces in the collimator lens mounts. The components are listed in Table 2. All surfaces are assumed to be black anodized aluminum with ε=0.88 and the scattering properties of black paint, a polynomial BRDF.

3.3   Field Lens Mounts

The field lens is the first optical element after the slit plane. The surfaces that are set up as thermal emitters are shown in **Figure 5**. The surfaces are all are black anodized aluminum with ε=0.88.
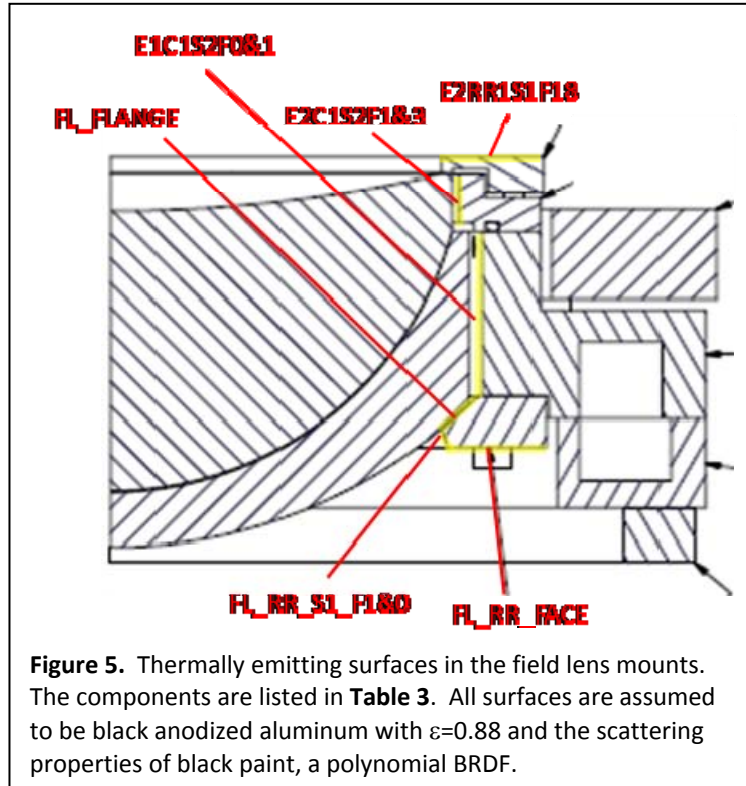

Figure 5. Thermally emitting surfaces in the field lens mounts. The components are listed in **Table 3**. All surfaces are assumed to be black anodized aluminum with ε=0.88 and the scattering properties of black paint, a polynomial BRDF.

Table 3. Thermally emitting surfaces in the field lens mounts.

Source	Label	Component
1	FL_RR_FACE	FL_RR_FACE
2	FL_RR_S1_F1&0	FL_RR_S1_F0
3	FL_RR_S1_F1&0	FL_RR_S1_F1
4	FL_FLANGE	FL_FLANGE
5	E1C1S2F0&1	Element_1_Cell_1_surface2_Face0
6	E1C1S2F0&1	Element_1_Cell_1_surface2_Face1
7	E2C1S2F1&3	Element_2_Cell_1_surface2_Face1
8	E2C1S2F1&3	Element_2_Cell_1_surface2_Face3
9	E2RR1S1F1	Element_2_Retaining_Ring_1_surface1_Face1
10	E2RR1S1F16	Element_2_Retaining_Ring_1_surface1_Face16
11	E2RR1S1F18	Element_2_Retaining_Ring_1_surface1_Face18

3.4 Waveplate Mounts

For spectroscopy mode observations the half waveplate will be out of the beam and the quarter waveplate will be in the clear compensator position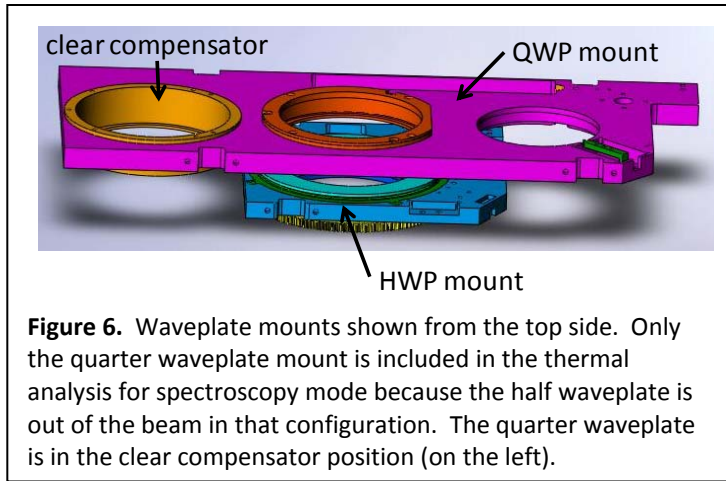. Therefore, only the quarter waveplate (QWP) is included in the thermal analysis. A compensator made of fused quartz with twice the thickness of a waveplate is in the clear position of the QWP mount.

Figure 6. Waveplate mounts shown from the top side. Only the quarter waveplate mount is included in the thermal analysis for spectroscopy mode because the half waveplate is out of the beam in that configuration. The quarter waveplate is in the clear compensator position (on the left).

The waveplate mounts are shown in **Figure 6**. Three parts are set up as thermal emitters: the top of the QWP mount, the top retaining ring of the clear compensator, and the bottom of the QWP mount. All are assumed to have ε=0.88, that of black anodized aluminum.

3.5 Optical Elements

3.5.1 Ambient Optics

Optical elements included in the ambient portion of the instrument are the field lens, the waveplate compensator, the common elements of the collimator, the dichroic beamsplitter, and the first element of the NIR doublet. These elements are listed with their assumed optical properties in **Table 4**. Emissivities are calculated with Equation (1), where α is the absorption coefficient per mm of the glass at λ = 1.7 μm and t is the thickness of the element. The absorption coefficients were taken from glass catalogs, or estimated from similar materials in the case of fused quartz.

$$\varepsilon = 1 - e^{-\alpha t}$$

(1)

Table 4. Optical elements and properties in the ambient temperature section of RSS-NIR.

Element	ASAP Label	Material	Radii (mm)	Thickness (mm)	n(λ) (0.9, 1.7 μm)	α (mm^{-1})	ε
Field lens #1	LENS_1.Z_11_12	fused quartz TOSOH	93.95, 64.2	10	1.45194882 1.44218867	5 e-5	0.0005
Field lens #2	LENS_1.Z_13_14	CaF$_2$	64.2, 266.58	51	1.42965613 1.425357297	2 e-6	0.0001
Waveplate compensator	PLT_2	Fused quartz	∞, ∞	23.96	1.45184721 1.442289604	5 e-5	0.0012
Collimator #1	LENS_2.Z_20_21	fused quartz TOSOH	-67.09, 198.89	10	1.45194882 1.44218867	5 e-5	0.0005
Collimator #2	LENS_3.Z_24_25	fused quartz TOSOH	-726.34, -140.99	30	1.45194882 1.44218867	5 e-5	0.0015
Collimator	LENS_4.Z_28_29	CaF$_2$	914.4,	55	1.42965613	2 e-6	0.0001

triplet #1			-133.1		1.425357297		
Collimator triplet #2	LENS_4.Z_30_31	NaCl	-133.1, -224.84	15	1.53366415 1.527619461	2.532 e-3	0.037
Collimator triplet #3	LENS_4.Z_32_33	CaF$_2$	-224.84, -141.12	37	1.42965613 1.425357297	2 e-6	0.00007
Dichroic beamsplitter	DBS	fused quartz	∞, ∞	10	1.45184721 1.442289604	5 e-5	0.0005
NIR doublet #1	LENS_5.Z_36_37	fused silica	∞, 187.77	15	1.45175396 1.44202000	1 e-3	0.015

Each optical element can contribute thermal radiation either from the second surface directly toward the detector, or from the first surface toward the slit, which can then be reflected back into the beam toward the detector. Therefore, thermal emission must be assigned to both sides of the optical elements. We do this by calculating emissivities for each surface using half of the total component thickness. This assumes that half of the radiation from an element is emitted in each direction, which may not be completely correct given specific lens geometries and the center thicknesses used to calculate emissivities, but should be close enough for our analysis.

3.5.2 Pre-Dewar Optics

The optical elements in the pre-dewar include the second lens in the NIR doublet, the fold mirror, the grating (or etalon and blocking filter for Fabry-Perot mode), the first three camera lenses, and the polarizing beamsplitter (only for polarimetry mode). Note that these analyses were all done with an earlier NIR collimator doublet and camera design. The current camera, which took the system from f/2 to f/1.4, contains one more element and slightly different materials. The new camera is not discussed in this report because its design was completed after these thermal analyses were done.

Table 5. Optical components housed in the pre-dewar, which will operate at -40 $^{\circ}$C.

Element	ASAP Label	Material	Radii (mm)	Thickness (mm)	n(λ) (0.9, 1.7 μm)	α (mm^{-1})	ε
NIR doublet #2	LENS_5.Z_38_39	CaF$_2$	187.77, -544.587	51	1.42965613 1.425357297	2 e-6	0.0001
Fold mirror	FM	Al	∞	---	---	---	0.06
Grating	G1	fused quartz	∞	20	1.45184721 1.442289604	5 e-5	0.001
Polarizing beamsplitter		calcite					
Camera #1	LENS_6.Z_43_44	CaF$_2$	291.00, -327.36	43	1.42965613 1.425357297	2 e-6	0.00009
Camera #2	LENS_7.Z_45_46	S-LAM66	-291.78, -829.03	7	1.78122433 1.740000000	3 e-4	0.002
Camera #3	LENS_8.Z_47_48	CaF$_2$	170.65, -331.61	52	1.42965613 1.425357297	2 e-6	0.0001
Camera #4	LENS_9.Z_49_50	Silica	-222.83, -1942.54	10	1.45175395 1.44202000	1 e-3	0.0099
Camera #5	LENS_10.Z_51_52	I-FPL51Y	83.27, 442.82	13	1.49125332 1.48486000	1.5 e-4	0.002
Camera #6	LENS_11.Z_53_54	S-LAM66	-163.31, 164.26	4	1.78122433 1.740000000	3 e-4	0.0012

4 Pre-Dewar

The pre-dewar contains all mounts for the optics in the previous section, along with mechanisms for inserting the gratings, etalons, blocking filters, and polarizing beamsplitter into the beam, as shown in **Figure 1**. However, to get an initial estimate of the required operating temperature of the pre-dewar before the mechanical designs were mature, we used a conceptual design of the pre-dewar enclosure, and assumed that all components within the enclosure reached the stated pre-dewar temperature. **Figure 7** shows a top view of the conceptual pre-dewar used in our ASAP thermal model. The cyan structure is the pre-dewar enclosure,

Figure 7. Conceptual model of pre-dewar components.

the blue background is the telescope primary mirror, the white circles are the SAC mirrors, and the purple square is the NIR fold mirror. The blue arrows are rays that reflect off of the fold mirror to the angled grating where they get diffracted to the camera and inside the dewar to the detector. A fraction of the rays are also transmitted through the grating and scatter off of the pre-dewar walls.
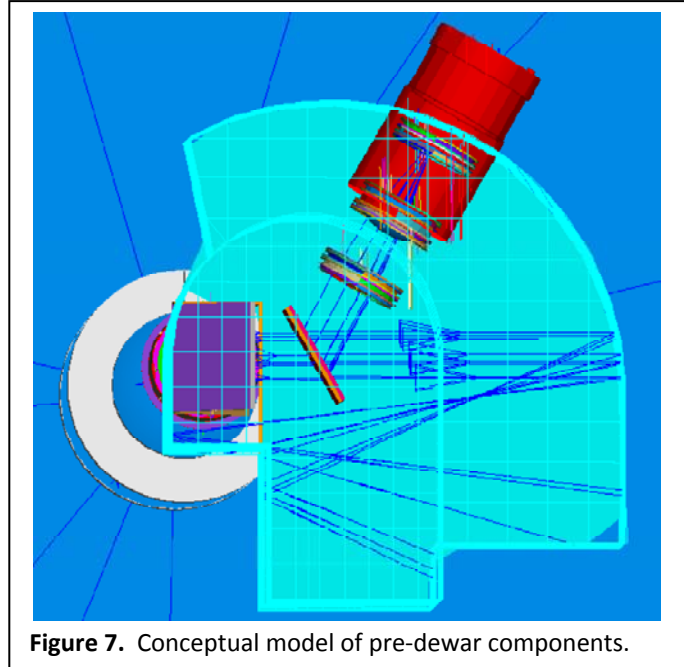
4.1 Initial Estimates

The thermal emission reaching the detector for a cutoff wavelength of λ_{cutoff} = 1.7 μm is shown in **Figure 8** as a function of pre-dewar temperature. All ambient temperature components shown are assumed to be at a temperature of +20 ^{o}C. Based on these estimates, a working operating
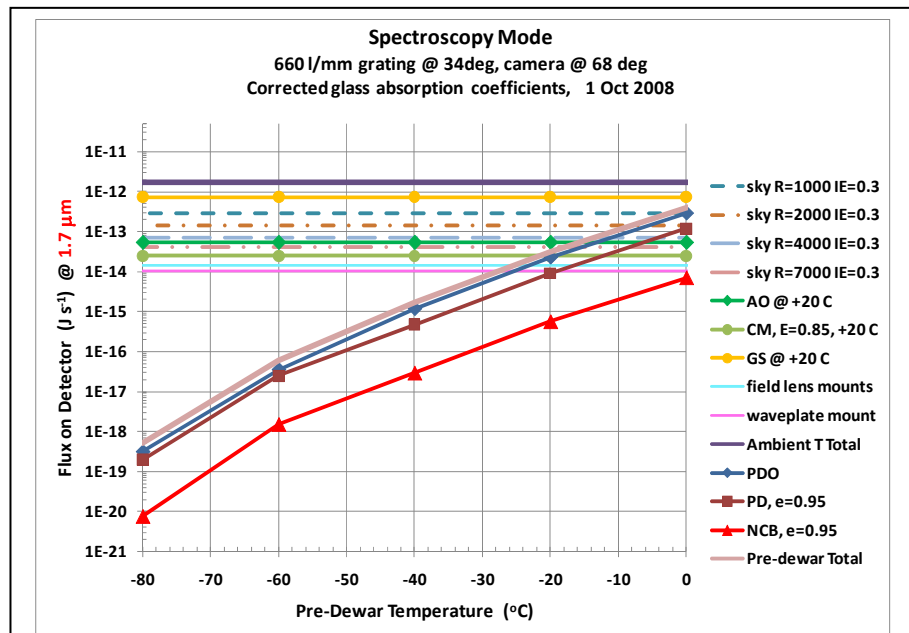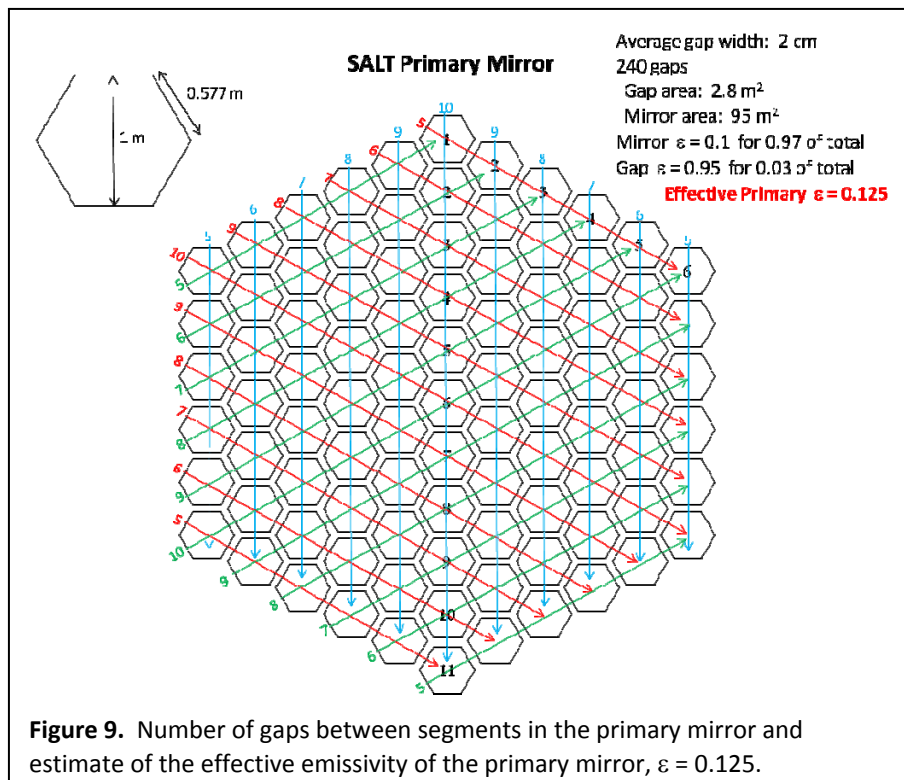

Figure 8. Preliminary estimates of pre-dewar operating temperature. This plot shows the thermal emission from instrument components that reaches the detector as a function of the pre-dewar temperature. **PDO** is the optical components in the pre-dewar, **PD** is the pre-dewar enclosure itself, and **NCB** is the NIR camera barrel lens mounts. Ambient temperature components are assumed to be at T_{amb} = +20 ^{o}C. **AO** is the ambient optics, **CM** is the collimator mounts, and **GS** is the gold long slit. Sky continuum levels at the detector are shown for a range of spectral resolutions, assuming an instrument efficiency of 0.3.

13

temperature of -40 °C was chosen for the pre-dewar. This put the total background from the pre-dewar components a factor of ~5 below the lowest ambient temperature component, and ~20 below the sky at R=7000. Mil specs for many mechanisms go down to -50 °C, so -40 °C also seemed to be a reasonable level from the operational side.

5 Telescope

The telescope is modeled in ASAP as a circular primary mirror with 11 meter diameter, but including the effective thermal emissivity of the actual gaps between segments. The estimate of this emissivity, scaled by relative areas of segments and gaps, is shown in **Figure 9**. A mirror emissivity of ε = 0.1 is assumed for both the primary mirror segments and the spherical aberration corrector (SAC) mirrors, to simulate dirty mirrors. The effective value for the primary mirror with gaps between segments is ε = 0.125.

Two configurations are analyzed in ASAP: one with the payload centered above the spherical primary, and one at the tracker extremes of angle and translation such that the pupil is partially off of the primary mirror. In the second case, the floor emits with ε = 1. These two configurations are shown in **Figure 10**. Components included in the analysis are listed in **Table 6** with the assumed thermal emissivities. As a worst case estimate, this analysis does not include the telescope moving baffle to mask the floor.
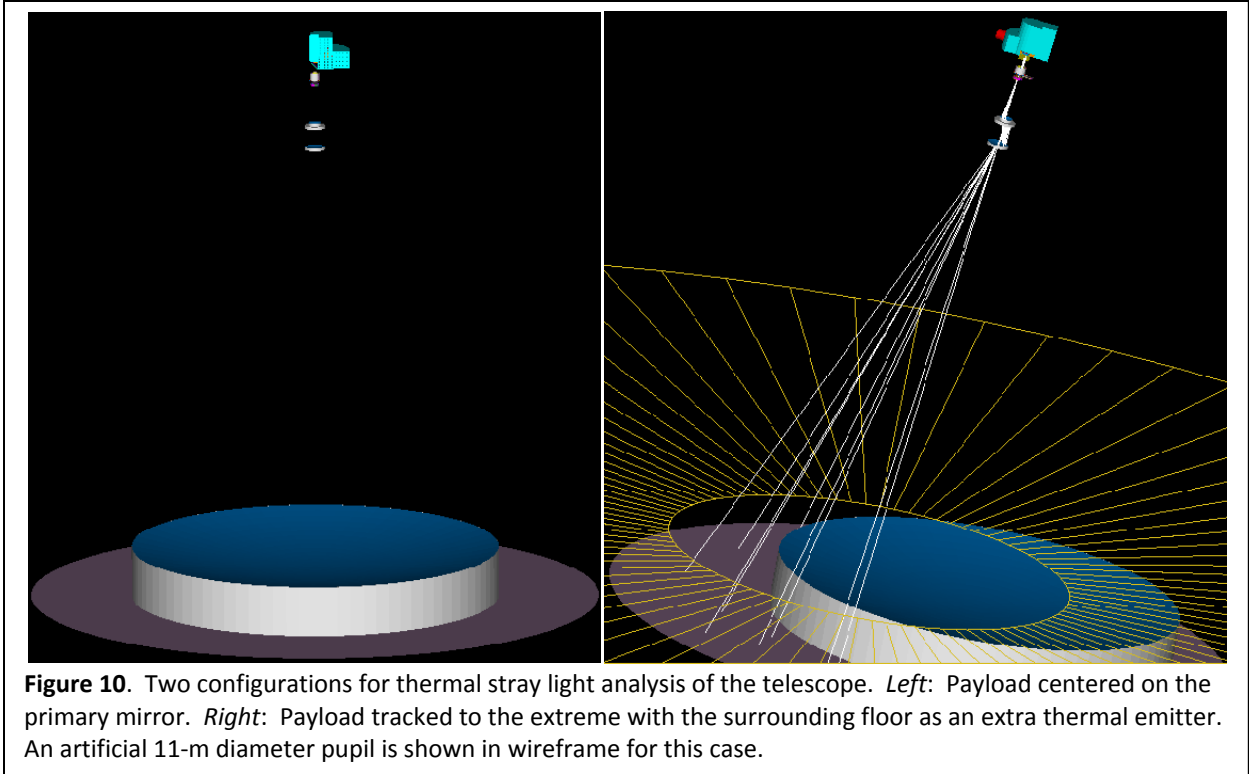

Figure 9. Number of gaps between segments in the primary mirror and estimate of the effective emissivity of the primary mirror, ε = 0.125.

Figure 10. Two configurations for thermal stray light analysis of the telescope. *Left*: Payload centered on the primary mirror. *Right*: Payload tracked to the extreme with the surrounding floor as an extra thermal emitter. An artificial 11-m diameter pupil is shown in wireframe for this case.

Table 6. Components in the telescope model.

Element	ASAP Label	Emissivity
Primary mirror	PM.Z_1	0.125
mirror segments		0.1
segment gaps		0.95
SAC M2	SM.Z_3	0.1
SAC M3	TM.Z_4	0.1
SAC M4	QM.Z_7	0.1
SAC M5	MIR_5.Z_8	0.1
Back of M2	SM.BACK_3	0.95
Back of M4	QM.BACK_7	0.95
Floor around primary	FLOOR	1.0

6   Thermal Analysis

The conceptual ASAP model of RSS-NIR is shown in **Figure 11**. The optical components were imported from Zemax and the mechanical components were imported from SolidWorks. In this figure the instrument is configured for grating spectroscopy at the longest wavelength, $\lambda = 1.7\ \mu m$, with the grating at an angle of 34° and the camera articulated to 68° (see grating efficiency contours in **Figure 13**).
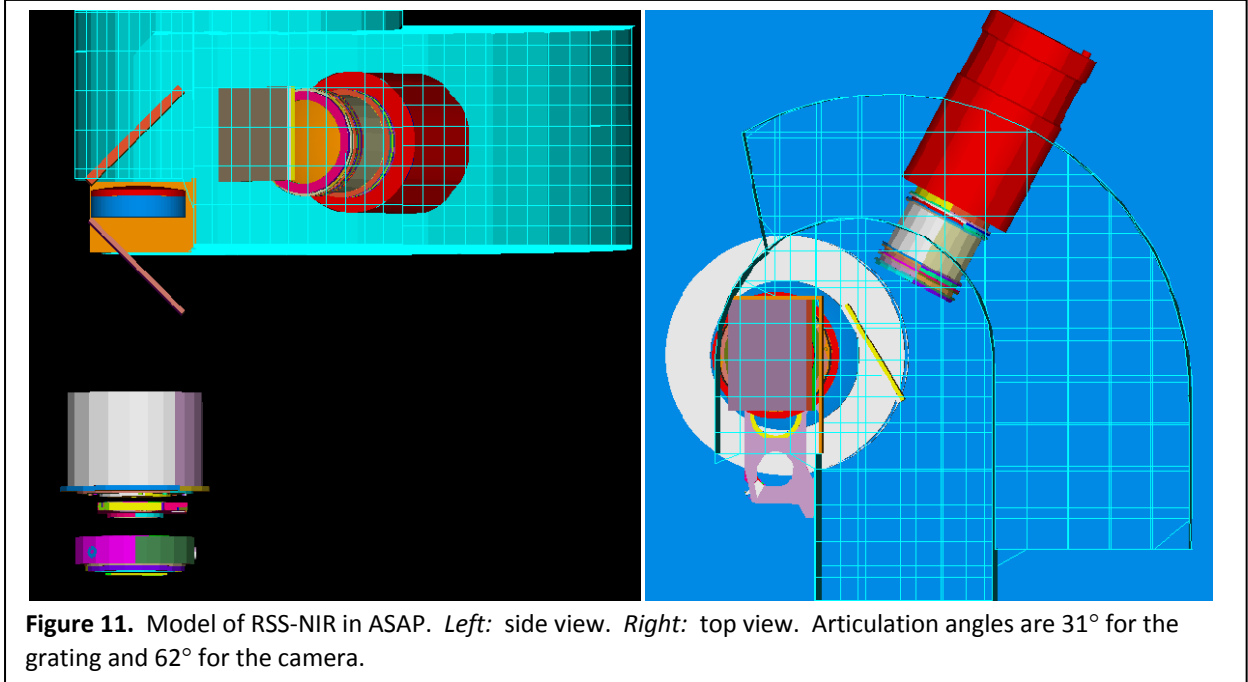
Figure 11. Model of RSS-NIR in ASAP. *Left:* side view. *Right:* top view. Articulation angles are 31° for the grating and 62° for the camera.

6.1   Calibration of ASAP

As an initial calibration, we checked the results of the ASAP ray traces against two independent back of the envelope (BOE) calculations of the thermal emission from the slit assembly that reaches the detector with the instrument in imaging configuration (no grating in place, no camera articulation). The first BOE calculation was performed by Wolf. She constructed a simple Mathcad model in which a Hawaii-2RG detector array with A_{det} = (18 μm x 2048)^2 = 1359 mm^2 receives light from our camera via an f/2.025 beam (focal length = 302 mm) over the wavelength range of λ = 0.8 – 2.5 μm. The thermal radiation at each wavelength is calculated as the blackbody integral between λ_{min} and λ_{max}, as given in Equation (2). N_{TB} is the thermal background in e^- s^{-1}, η_{det} is a detector efficiency factor (set to 1), F_λ is the optics transmission (set to 1), h is the Planck constant, c is the speed of light, k is the Boltzmann constant, and *T1* is the ambient temperature.

$$N_{TB} = A_{det} \cdot \Omega \cdot \int_{\lambda_1}^{\lambda_2} \eta_{det} \cdot F_\lambda \cdot \left(\frac{2 \cdot c}{\lambda^4 \cdot \exp\left(\frac{h \cdot c}{\lambda \cdot k \cdot T1} - 1 \right)} \right) d\lambda$$

(2)

Results from the Wolf BOE calculation are shown in **Figure 12** for temperatures of 0 °C and -80 °C. At λ = 1.7 μm and T_{amb} = 0 °C, the thermal background rate at the detector is 1.7 x 10^{-6} e^- s^{-1} pixel^{-1}, or 1.67 x 10^{-16} J s^{-1} mm^{-2}, converting it to the default units used in ASAP. At λ = 1.3 μm, the background rate is 2.65 x 10^{-20} J s^{-1} mm^{-2}.

Figure 12. BOE calculation of thermal background reaching the detector.
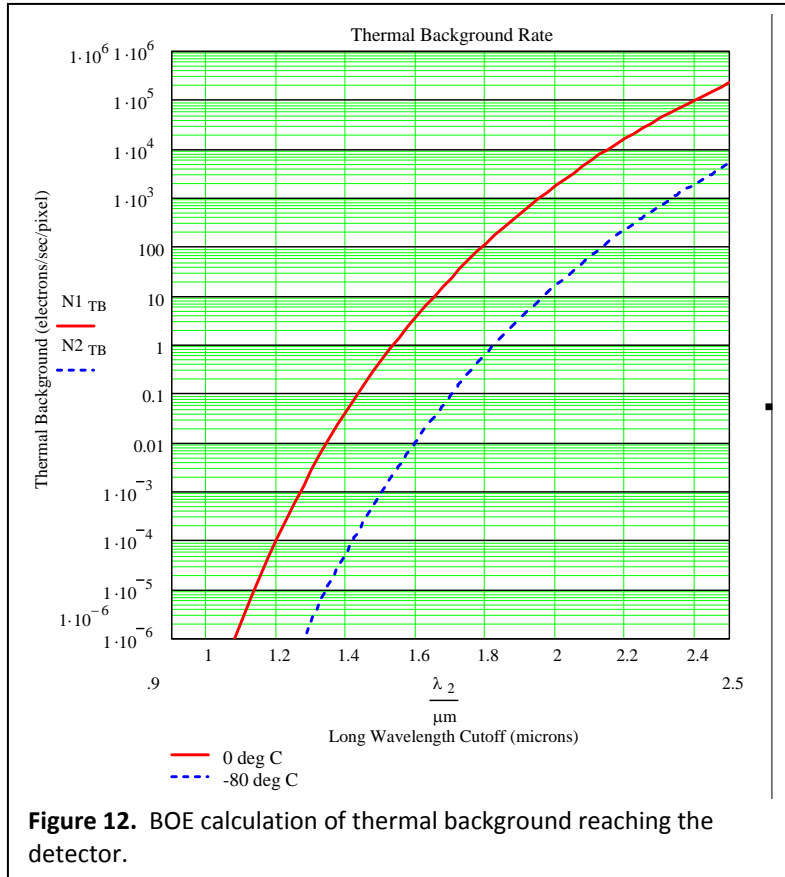
An ASAP ray trace of thermal emission from the long slit assembly results in a background level of 1.68×10^{-16} J s^{-1} mm^{-2} at $\lambda = 1.7\ \mu$m at the detector plane. For this ray trace, all optical coatings were set to be completely transmitting since no optical losses were assumed in the BOE calculation.

6.2   Spectroscopy Mode

We began with analysis of the spectroscopy modes of the instrument, since sky-limited spectroscopy of faint targets at high resolution will be the observations most affected by the instrument thermal background preventing us from reaching the sky continuum limit. Spectroscopy mode observing is classical grating spectroscopy using volume phase holographic gratings (VPHGs). To take advantage of the superblaze efficiency function of these gratings, the grating and camera articulate (0 to 50° for the grating and 0 to 100° for the camera). The initial proposed suite of gratings for RSS-NIR (at the time of PDR) is shown in **Figure 13**. Because the longest wavelength in the spectral range contributes the most instrument thermal background, the thermal analysis for this observing mode is done for a configuration that has high efficiency at our long wavelength cutoff of $\lambda = 1.7\ \mu$m. At this wavelength we chose a configuration with the 660 l/mm grating at an angle of 34° and the camera at an angle of 68° as the default for analysis.
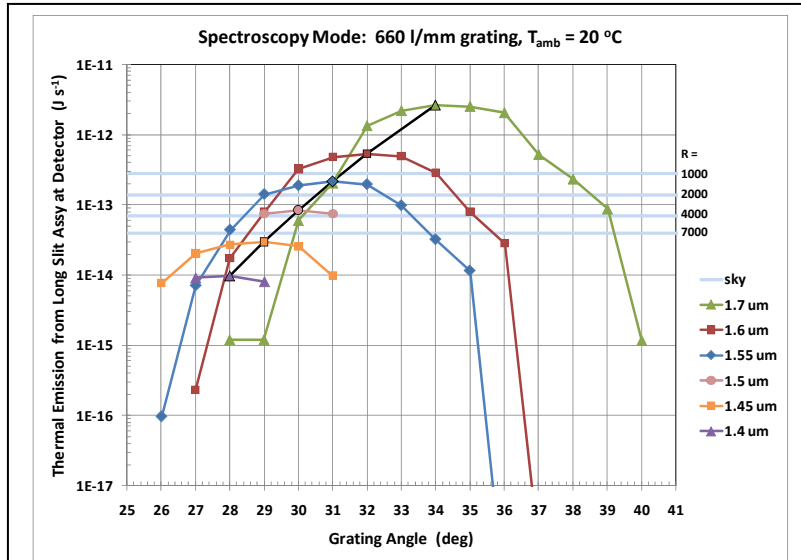

Figure 13. Proposed grating suite for RSS-NIR when these analyses were done (at the time of PDR).
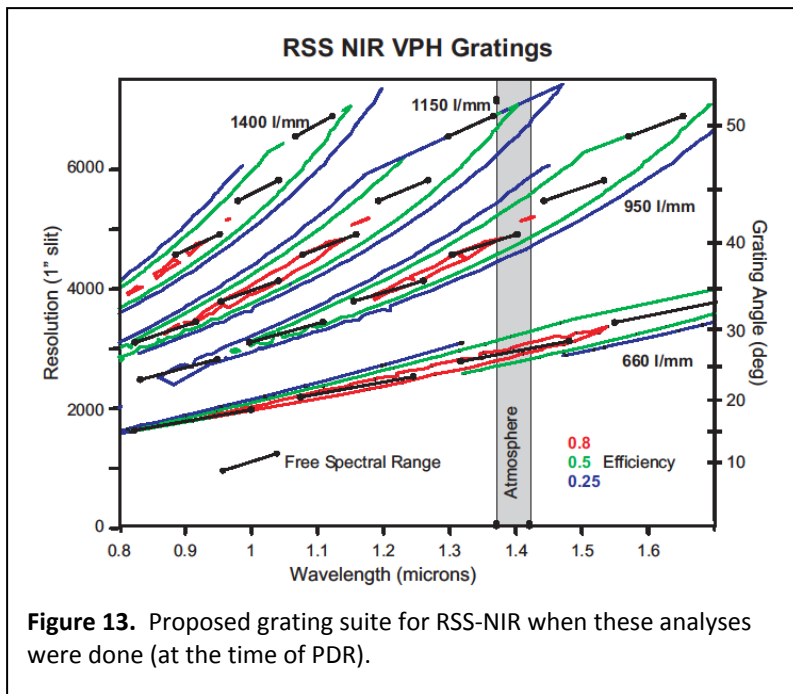
Figure 14. Thermal background from the long slit assembly with the 660 l/mm grating set at different angles. Sky background levels are shown as horizontal lines for R = 1000, 2000, 4000, and 7000 (see Section 6.3). The maximum flux points at all wavelengths are connected by the black line.

For analyzing instrument thermal backgrounds at shorter cutoff wavelengths we need to tune the grating to the optimum coupling angle for each wavelength. To exactly determine the most efficient grating angles we ran a series of quick ray traces (1000 rays for each emitting surface, rather than the standard 10,000 rays) for slit emission at different grating angles. The results are shown in **Figure 14** for an ambient temperature of +20 °C. The flux at the detector will go down by approximately a factor of 10 per ΔT_{amb} = -20 °C. Optimum coupling angles for the 660 l/mm grating are 28°, 29°, 30°, 31°, 32°, and 34° for λ_c = 1.4, 1.45, 1.5, 1.55, 1.6, and 1.7 μm, respectively.
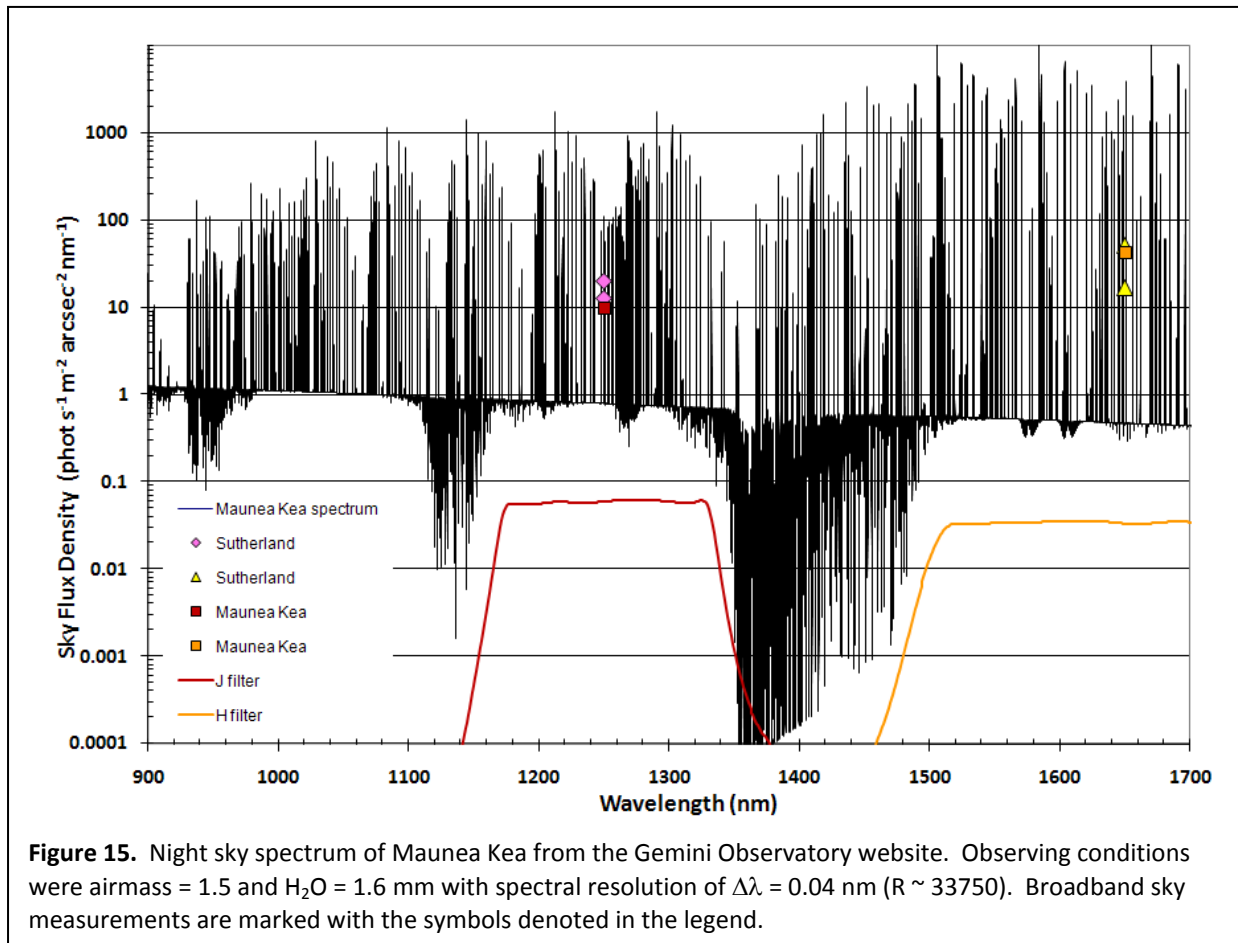
6.3 NIR Sky Background

High resolution NIR spectra of the SALT site at Sutherland do not exist. Therefore, we use data from Maunea Kea in Hawaii, shown in **Figure 15**. Broadband measurements from both sites are taken from Taka Nagayama's thesis and shown as symbols. Values are given in **Table 7**. Because the broadband measurements are close, and for lack of better information, we think it is reasonable to use the Maunea Kea night sky for estimating sky backgrounds for SALT. We smooth this spectrum to the proposed resolutions available on RSS-NIR and take the sky continuum levels for each in between OH emission lines near 1.7 μm. These sky values are multiplied by the estimated instrument throughput, 0.3, and used for comparison to our instrument thermal backgrounds throughout the analysis. Sky continuum values at λ = 1.7 μm with instrument efficiency applied are given in **Table 8**.

Table 7. Broadband measurements of the NIR night sky (from Taka Nagayama's thesis).

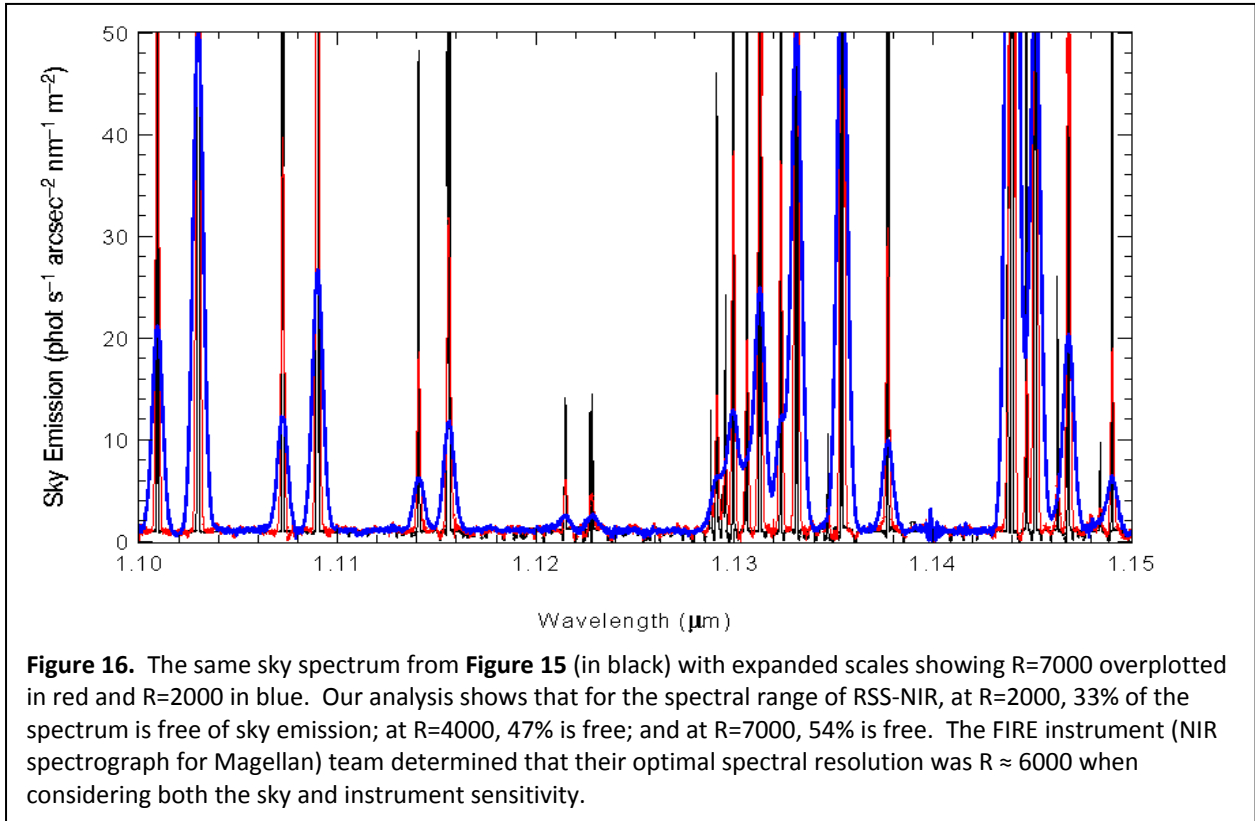| Site	J (mag)	H (mag)	Ks (mag)	Source
Mauna Kea	15.6	13.6	13.4	UKIRT/UFTI (web)
Sutherland	15.0 – 15.5	13.2 – 14.4	12.0 – 13.2	IRSF/SIRIUS (thesis)

Table 8. Sky continuum levels at λ = 1.7 μm for different spectral resolving powers.

Resolution (R)	1000	2000	4000	7000	8000
Sky cont. (W)	2.80033E-13	1.40512E-13	7.02588E-14	4.02132E-14	3.5206E-14

Figure 15. Night sky spectrum of Maunea Kea from the Gemini Observatory website. Observing conditions were airmass = 1.5 and H_2O = 1.6 mm with spectral resolution of $\Delta\lambda$ = 0.04 nm (R ~ 33750). Broadband sky measurements are marked with the symbols denoted in the legend.

6.3.1   Spectral Resolution

Because we will be providing gratings at low spectral resolutions for use on bright objects, a discussion of resolution in the presence of night sky emission lines is important. We smooth the night sky emission spectrum to spectral resolutions of interest and plot them in **Figure 16**. At R < 4000 the majority of night sky lines are blended and observations of objects cannot reach the true sky continuum between these lines. This is fine for bright objects, but not for faint sky-limited observations. Simulations for the FIRE instrument on the Magellan Telescope have shown that only at R > 3500 is less than half of the J-band affected by night sky lines. They find an optimal resolution of R ≈ 6000 when considering both the sky and instrument sensitivity. Our analysis shows that over the RSS-NIR spectral range of λ = 0.9 – 1.7 μm, at R=2000, 33% of the spectrum is free of sky emission lines; at R=4000, 47% is free; and at R=7000, 54% is free. Therefore, although upcoming plots may show that our instrument background is below the sky continuum at low spectral resolutions, this continuum is contaminated by sky emission lines over most of the range and not the actual sky minimum between lines. Observations of faint objects should be made at R ≥ 4000 to achieve the true sky continuum limit within specific atmospheric windows.

Figure 16. The same sky spectrum from **Figure 15** (in black) with expanded scales showing R=7000 overplotted in red and R=2000 in blue. Our analysis shows that for the spectral range of RSS-NIR, at R=2000, 33% of the spectrum is free of sky emission; at R=4000, 47% is free; and at R=7000, 54% is free. The FIRE instrument (NIR spectrograph for Magellan) team determined that their optimal spectral resolution was R ≈ 6000 when considering both the sky and instrument sensitivity.

6.4   Identification of Critical Objects

The first step in an ASAP analysis is to identify all the critical objects in the system. This is done by placing an emitting source at the detector and ray tracing backwards through the system. Once this is done a list can be generated that contains the geometrical configuration factors (GCF), or view factors, of all surfaces that the detector sees. These factors can be used to gauge the relative importance of each surface to be considered as a thermal emitter in the system. Critical objects for our system are given in **Table 9**.

Table 9. Critical objects identified in ASAP, sorted by GCF.

Object #	# Rays	GCF	Object name in ASAP
377	2280	295.0483	LENS_11.Z_53
379	2080	269.8813	LENS_11.EDGE_53_54
229	1584	177.6527	Default.NIR OPTICS BODY-2-surface1.Face1
228	1512	169.965	Default.NIR OPTICS BODY-2-surface1.Face0
376	775	90.13571	LENS_10.EDGE_51_52
248	636	82.95987	Default.ND-10_WISC_CONCEPT_MODEL_4-1/PART1-1-surface1.Face18
250	619	81.10886	Default.ND-10_WISC_CONCEPT_MODEL_4-1/PART1-1-surface1.Face20
240	618	81.0479	Default.ND-10_WISC_CONCEPT_MODEL_4-1/PART1-1-surface1.Face10
238	618	80.71067	Default.ND-10_WISC_CONCEPT_MODEL_4-1/PART1-1-surface1.Face8
236	615	80.38665	Default.ND-10_WISC_CONCEPT_MODEL_4-1/PART1-1-surface1.Face6
254	613	80.28001	Default.ND-10_WISC_CONCEPT_MODEL_4-1/PART1-1-surface1.Face24
252	602	78.66436	Default.ND-10_WISC_CONCEPT_MODEL_4-1/PART1-1-surface1.Face22

Object #	# Rays	GCF	Object name in ASAP
246	604	78.19604	Default.ND-10_WISC_CONCEPT_MODEL_4-1/PART1-1-surface1.Face16
242	457	59.70745	Default.ND-10_WISC_CONCEPT_MODEL_4-1/PART1-1-surface1.Face12
237	452	59.25385	Default.ND-10_WISC_CONCEPT_MODEL_4-1/PART1-1-surface1.Face7
233	428	55.77671	Default.ND-10_WISC_CONCEPT_MODEL_4-1/PART1-1-surface1.Face3
244	428	55.63499	Default.ND-10_WISC_CONCEPT_MODEL_4-1/PART1-1-surface1.Face14
234	426	55.41135	Default.ND-10_WISC_CONCEPT_MODEL_4-1/PART1-1-surface1.Face4
239	424	54.96481	Default.ND-10_WISC_CONCEPT_MODEL_4-1/PART1-1-surface1.Face9
241	406	53.3179	Default.ND-10_WISC_CONCEPT_MODEL_4-1/PART1-1-surface1.Face11
235	387	50.38651	Default.ND-10_WISC_CONCEPT_MODEL_4-1/PART1-1-surface1.Face5
243	317	35.35789	Default.ND-10_WISC_CONCEPT_MODEL_4-1/PART1-1-surface1.Face13
373	233	25.9261	LENS_9.BACK_PLANE_Z_50
225	245	23.37611	Default.NIR OPTICS BODY-1-surface1.Face2
301	453	22.44098	PM.Z_1
224	223	20.88611	Default.NIR OPTICS BODY-1-surface1.Face1
372	131	14.01043	LENS_9.EDGE_49_50
369	126	13.24288	LENS_8.BACK_PLANE_Z_48
316	199	8.725787	MIR_5.BACK_8
3	88	6.367104	DM.EDGE
306	80	5.759573	SM.BACK_3
223	54	5.258392	Default.NIR OPTICS BODY-1-surface1.Face0
310	119	5.218099	TM.BACK_4
226	54	5.163016	Default.NIR OPTICS BODY-1-surface1.Face3
313	104	4.560789	QM.BACK_7
15	59	4.162119	Default.PFIS COLLIMATOR ASSEMBLY 090703-1/PFIS COLIMATOR ELEMENT 7 CELL-1-surface1.Face2
42	54	3.878713	Default.PFIS COLLIMATOR ASSEMBLY 090703-1/COLIMATOR BARREL BLADDER COVER-1-surface1.Face11
222	51	3.790533	FM.EDGE
2	49	3.670911	DM.BACK
351	42	3.116849	LENS_5.Z_36
368	28	2.787236	LENS_8.EDGE_47_48
364	28	2.519003	LENS_7.FRONT_PLANE_Z_45
361	17	1.419935	LENS_6.BACK_PLANE_Z_44
51	19	1.281411	Default.PFIS COLLIMATOR ASSEMBLY 090703-1/COLLIMATORFLANGEINTERFACE-1-surface1.Face3
203	160	1.131581	Default.PFIS Field Lens Assembly 082603-1/Field Lens Element 1 Retaining Ring-1-surface1.Face2
360	14	1.10969	LENS_6.EDGE_43_44
7	243	1.097504	Default.PFIS COLLIMATOR ASSEMBLY 090703-1/CELL 2 SEAT-1-surface1.Face3
319	20	1.073534	LENS_1.EDGE_11_12
179	20	1.050718	Default.PFIS Field Lens Assembly 082603-1/PFIS Field Lens Element 2 Retaining Ring-1-surface1.Face18
55	14	1.017841	Default.PFIS COLLIMATOR ASSEMBLY 090703-1/COLLIMATORFLANGEINTERFACE-1-surface1.Face7
52	24	0.861514	Default.PFIS COLLIMATOR ASSEMBLY 090703-1/COLLIMATORFLANGEINTERFACE-1-surface1.Face4
311	16	0.701493	QM.Z_7

Object #	# Rays	GCF	Object name in ASAP
357	14	0.564417	LENS_5.EDGE_38_39
28	9	0.563395	Default.PFIS COLLIMATOR ASSEMBLY 090703-1/PFIS COLIMATOR ELEMENT 7 RETAINING RING-1-surface1.Face2
53	7	0.50556	Default.PFIS COLLIMATOR ASSEMBLY 090703-1/COLLIMATORFLANGEINTERFACE-1-surface1.Face5
353	33	0.374565	LENS_5.EDGE_36_37
365	4	0.355342	LENS_7.EDGE_45_46
324	5	0.276372	LENS_1.FRONT_PLANE_Z_13
32	4	0.275513	Default.PFIS COLLIMATOR ASSEMBLY 090703-1/COLIMATOR BARREL BLADDER COVER-1-surface1.Face1
312	6	0.263085	QM.EDGE_7
378	2	0.21968	LENS_11.Z_54
120	199	0.162256	Default.PFIS COLLIMATOR ASSEMBLY 090703-1/PFIS COLLIMATOR ELEMENT 3 BEZEL-1-surface1.Face6
201	7	0.137067	Default.PFIS Field Lens Assembly 082603-1/Field Lens Element 1 Retaining Ring-1-surface1.Face0
33	2	0.131792	Default.PFIS COLLIMATOR ASSEMBLY 090703-1/COLIMATOR BARREL BLADDER COVER-1-surface1.Face2
227	1	9.64E-02	Default.NIR OPTICS BODY-1-surface1.Face4
202	7	9.20E-02	Default.PFIS Field Lens Assembly 082603-1/Field Lens Element 1 Retaining Ring-1-surface1.Face1
304	2	8.77E-02	SM.Z_3
323	256	8.04E-02	LENS_1.Z_14
210	519	7.78E-02	Default.PFIS Field Lens Assembly 082603-1/PFIS Field Lens Bladder Cover-1-surface1.Face5
106	2	7.39E-02	Default.PFIS COLLIMATOR ASSEMBLY 090703-1/PFIS COLIMATOR ELEMENT 4 RETAINING RING 2-1-surface1.Face0
112	1	7.28E-02	Default.PFIS COLLIMATOR ASSEMBLY 090703-1/PFIS COLIMATOR ELEMENT 4 RETAINING RING 2-1-surface1.Face6
50	10	7.06E-02	Default.PFIS COLLIMATOR ASSEMBLY 090703-1/COLLIMATORFLANGEINTERFACE-1-surface1.Face2
90	1	7.04E-02	Default.PFIS COLLIMATOR ASSEMBLY 090703-1/BELLEVILLE B0637-032-12-surface1.Face1
89	1	7.04E-02	Default.PFIS COLLIMATOR ASSEMBLY 090703-1/BELLEVILLE B0637-032-12-surface1.Face0
88	1	7.04E-02	Default.PFIS COLLIMATOR ASSEMBLY 090703-1/DIN 912_M6 X 1_100_NONE-12-surface1.Face0
218	1524	2.20E-02	Default.PFIS Field Lens Assembly 082603-1/PFIS Field Lens Element 1 Protective Ring-1-surface1.Face6
211	358	1.63E-02	Default.PFIS Field Lens Assembly 082603-1/PFIS Field Lens Bladder Cover-1-surface1.Face6
205	425	1.50E-02	Default.PFIS Field Lens Assembly 082603-1/PFIS Field Lens Bladder Cover-1-surface1.Face0
57	14	1.31E-02	Default.PFIS COLLIMATOR ASSEMBLY 090703-1/COLLIMATORFLANGEINTERFACE-1-surface1.Face9
180	20	1.24E-02	Default.PFIS Field Lens Assembly 082603-1/PFIS Field Lens Element 2 Retaining Ring-1-surface2.Face0
333	10	1.03E-02	LENS_2.EDGE_20_21
187	66	7.40E-03	Default.PFIS Field Lens Assembly 082603-1/PFIS Field Lens Element 2 Cell-1-

Object #	# Rays	GCF	Object name in ASAP
			surface2.Face3
11	9	6.89E-03	Default.PFIS COLLIMATOR ASSEMBLY 090703-1/PFIS COLLIMATOR SHIM RING-1-surface1.Face0
161	10	6.77E-03	Default.PFIS Field Lens Assembly 082603-1/PFIS Field Lens Element 2 Retaining Ring-1-surface1.Face0
162	9	6.60E-03	Default.PFIS Field Lens Assembly 082603-1/PFIS Field Lens Element 2 Retaining Ring-1-surface1.Face1
177	6	6.55E-03	Default.PFIS Field Lens Assembly 082603-1/PFIS Field Lens Element 2 Retaining Ring-1-surface1.Face16
178	7	5.88E-03	Default.PFIS Field Lens Assembly 082603-1/PFIS Field Lens Element 2 Retaining Ring-1-surface1.Face17
185	37	2.23E-03	Default.PFIS Field Lens Assembly 082603-1/PFIS Field Lens Element 2 Cell-1-surface2.Face1
125	1	2.14E-03	Default.PFIS COLLIMATOR ASSEMBLY 090703-1/BELLEVILLE B0637-032-13-surface1.Face0
314	2	1.93E-03	MIR_5.Z_8
221	1	1.93E-03	FM.BACK
212	547	1.88E-03	Default.PFIS Field Lens Assembly 082603-1/PFIS Field Lens Element 1 Protective Ring-1-surface1.Face0
128	1	1.80E-03	Default.PFIS COLLIMATOR ASSEMBLY 090703-1/BELLEVILLE B0637-032-14-surface1.Face1
383	9	1.75E-03	BAFFLE.T2
355	1	1.54E-03	LENS_5.EDGE_37_38
8	2	1.53E-03	Default.PFIS COLLIMATOR ASSEMBLY 090703-1/CELL 2 SEAT-1-surface1.Face4
149	2	1.34E-03	Default.PFIS Field Lens Assembly 082603-1/DIN 912_M4 X 0~7_16_NONE2-2-surface1.Face0
336	1	1.25E-03	LENS_3.EDGE_24_25
380	2	8.97E-04	FP.Z_56
382	21	8.67E-04	BAFFLE.T1
26	1	7.94E-04	Default.PFIS COLLIMATOR ASSEMBLY 090703-1/PFIS COLIMATOR ELEMENT 7 RETAINING RING-1-surface1.Face0
118	1	7.66E-04	Default.PFIS COLLIMATOR ASSEMBLY 090703-1/PFIS COLLIMATOR ELEMENT 3 BEZEL-1-surface1.Face4
331	1	7.61E-04	LENS_2.Z_21
194	1	6.01E-04	Default.PFIS Field Lens Assembly 082603-1/PFIS Field Lens Element 1 Cell-1-surface3.Face0
204	1	5.75E-04	Default.PFIS Field Lens Assembly 082603-1/Field Lens Element 1 Retaining Ring-1-surface2.Face0
209	3	2.54E-04	Default.PFIS Field Lens Assembly 082603-1/PFIS Field Lens Bladder Cover-1-surface1.Face4
54	14	2.40E-04	Default.PFIS COLLIMATOR ASSEMBLY 090703-1/COLLIMATORFLANGEINTERFACE-1-surface1.Face6
207	5	2.07E-04	Default.PFIS Field Lens Assembly 082603-1/PFIS Field Lens Bladder Cover-1-surface1.Face2
147	4	1.06E-04	Default.PFIS Field Lens Assembly 082603-1/DIN 912_M4 X 0~7_16_NONE2-1-surface1.Face0
148	2	3.41E-05	Default.PFIS Field Lens Assembly 082603-1/DIN 912_M4 X 0~7_16_NONE2-1-surface1.Face1
208	10	2.59E-05	Default.PFIS Field Lens Assembly 082603-1/PFIS Field Lens Bladder Cover-1-

Object #	# Rays	GCF	Object name in ASAP
			surface1.Face3
325	1	2.11E-05	LENS_1.EDGE_13_14
230	1	7.72E-07	Default.ND-10_WISC_CONCEPT_MODEL_4-1/PART1-1-surface1.Face0
359	1	3.63E-09	LENS_6.Z_44

---------	------	--	
	2407		
TOTAL	2	2326.301	

6.5   Results for Ambient Temperature Components

We analyze the thermal emitters in the system in groups to reduce computational time for each run and to simplify interpretation of the results. The groups within the ambient temperature common components are those described in Section 3. Results of the ray traces are shown in **Figure 17**. This is a plot of the flux that reaches the detector from each of the component groups, at a long wavelength cutoff of λ = 1.7 μm, as a function of the ambient temperature. The dashed horizontal lines mark the sky continuum levels for spectral resolutions of R = 1000, 2000, 4000, 7000 at λ = 1.7 μm, assuming an

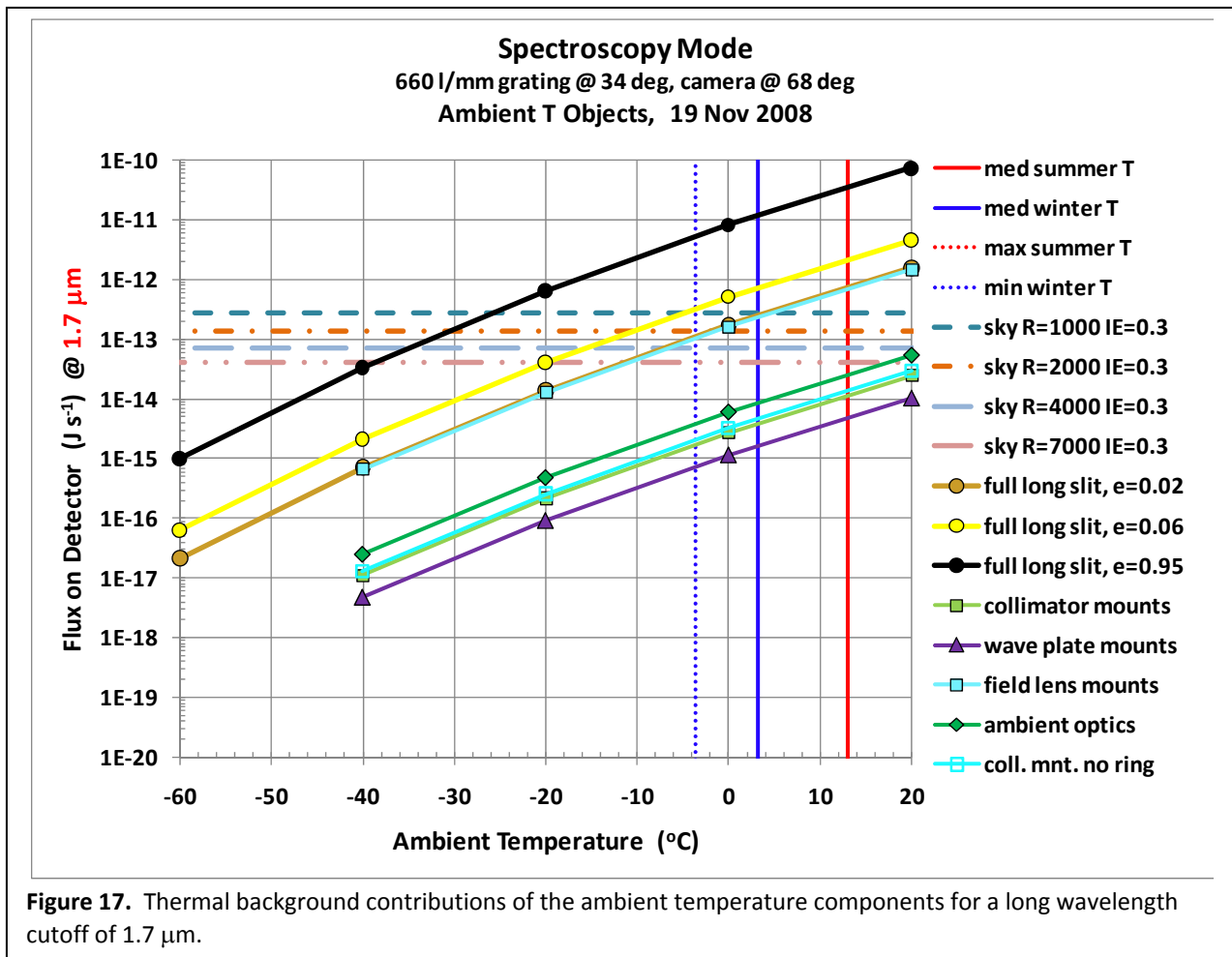**Figure 17.** Thermal background contributions of the ambient temperature components for a long wavelength cutoff of 1.7 μm.

instrument efficiency of 0.3. For sky-limited observations the total instrument background must be below the sky continuum level. The solid vertical lines mark the median winter and summer temperatures at SALT, and the dotted lines denote the minimum winter temperature and maximum summer temperature. The top black curve with filled circles is for a black long slit assembly with ε = 0.95, the yellow curve is for ε = 0.06 (that of aluminum), and the gold curve is for ε = 0.02 (that of gold). We see that even if the long slit assembly is gold-coated, sky-limited observations at λ = 1.7 μm would never be possible because the emission from the slit alone is at the sky limit for the lowest spectral resolution at the minimum winter temperature.

The rest of the curves show the background from the optics and mounts, as indicated in the legend. The slit assembly contributes the highest background of all components. Breakdown of this radiation by component is given in **Table 10** as a percentage of the total flux reaching the detector from the long slit assembly.

Table 10. Breakdown of thermal radiation at the detector from the long slit assembly.

Component	Percentage
beam covering part of slit blank	31.10
baffle on one side	23.83
inner indentation to slit location	20.18
1st indentation to slit location	15.06
flat top of slit blank	8.73
angled cut in top of slit blank	1.10
baffle on other side	0.00

6.5.1   Problem Component Identified

One component group to note in **Figure 17** is the field lens mount. The emission from this group is nearly as much as the slit. Upon investigation of where the rays originate, we see the reason in **Figure 18**. The bottom retaining ring follows the angle of the first element in the field lens. It is a 5 mm thick black anodized ring that emits straight into the highly curved lens surface and this radiation is refracted
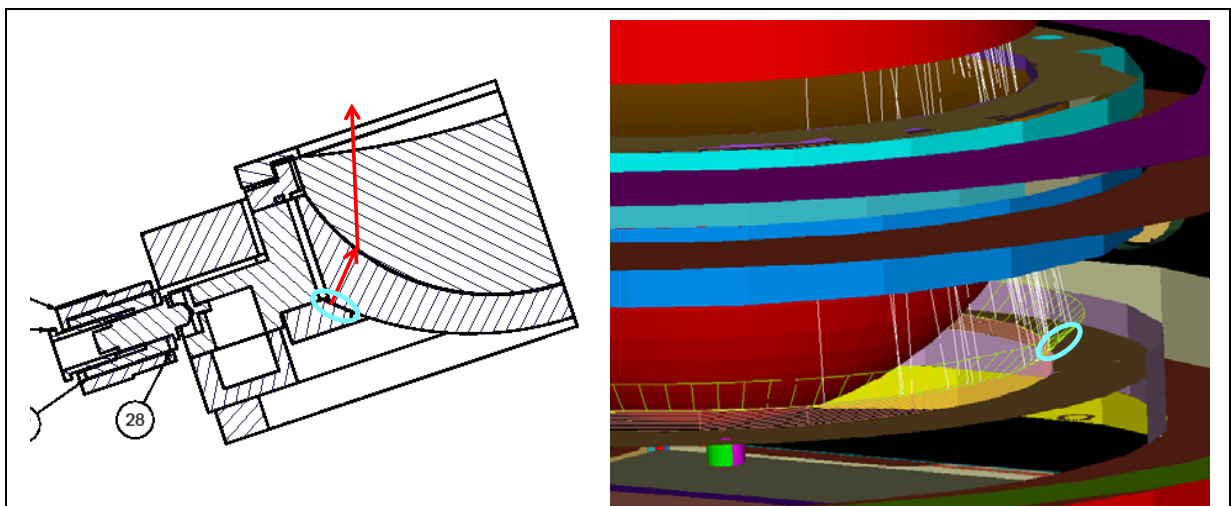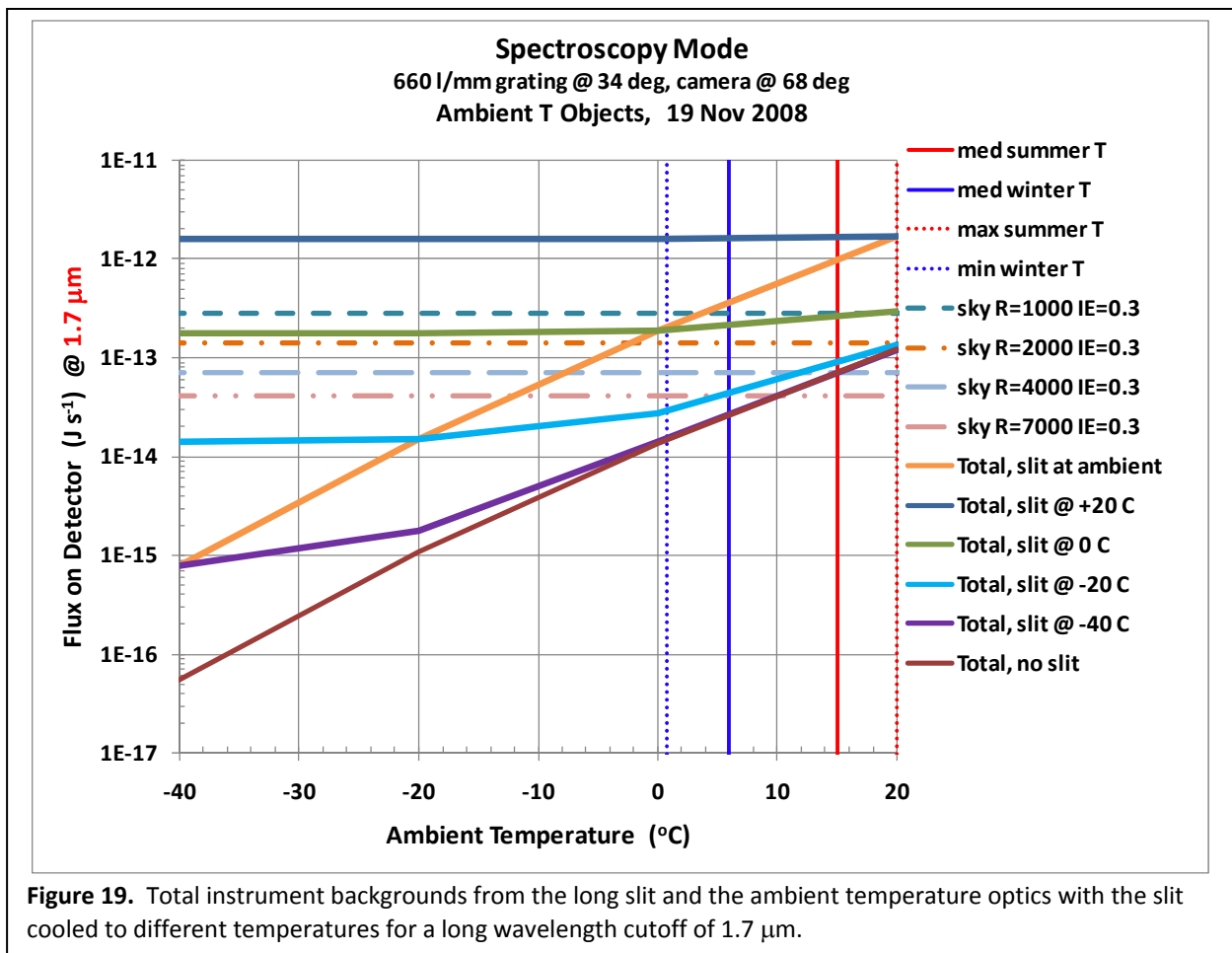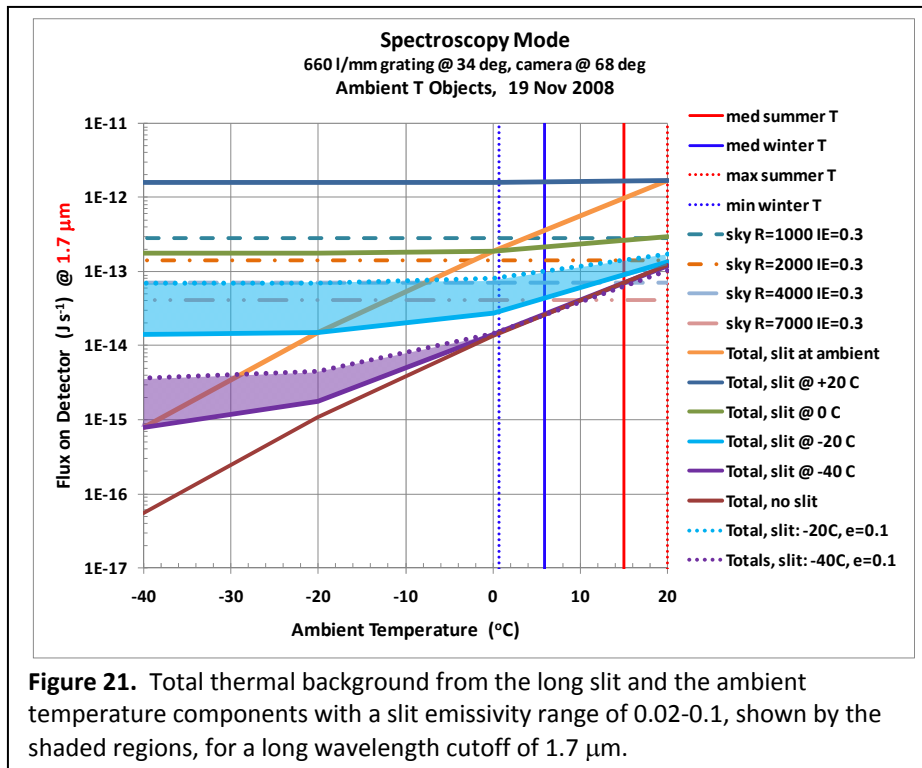

Figure 18. Thermal radiation directly coupled into the beam from one surface of the field lens mounts. The surface of the first element in the field lens has been hidden for clarity. The white lines are rays in ASAP.

into the center of beam and makes it through the entire system to the detector. ***This is a strong radiation path that likely would not have been identified before the instrument was built without the prior thermal stray light analysis in ASAP.*** We are having this ring cut down from a width of 5 mm to 2 mm and placing low emissivity gold foil on the surface facing the lens. We estimate that this will take the thermal emission down to that from other components. No surfaces in the collimator lens mounts seem to pose a similar problem because the radiation from them is not coupled into the beam nearly as efficiently as the field lens retaining ring case.
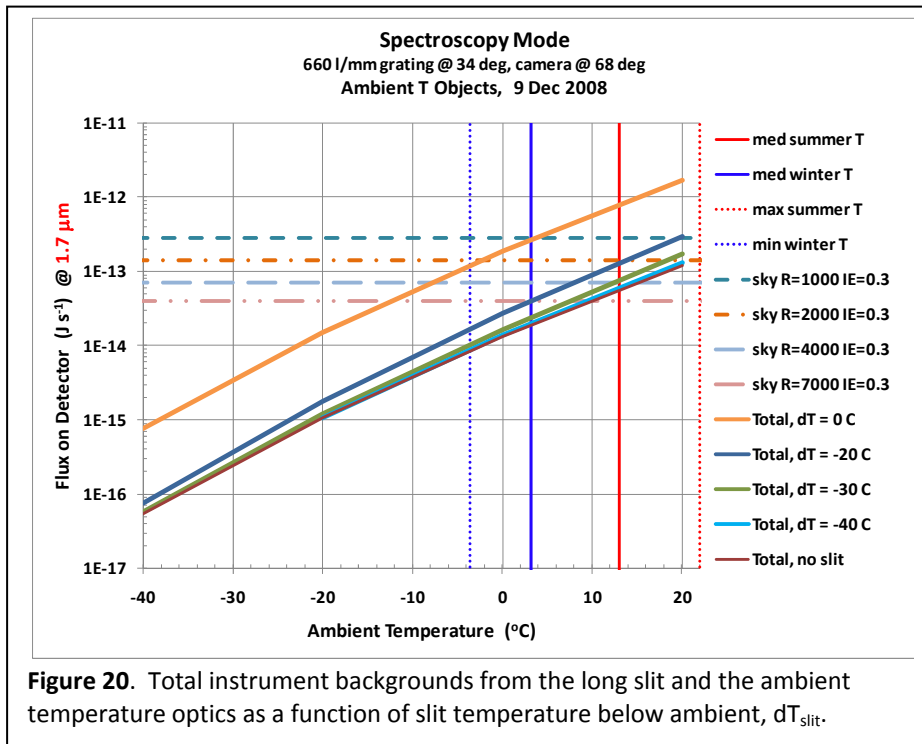
6.5.2   Slit Cooling

Because the slit is the limiting factor, we now investigate the effects of cooling it. If we assume that the field lens mount modification will make the thermal background from the first retaining ring negligible, total backgrounds reaching the detector are shown in **Figure 19**. The upper orange curve is the total radiation reaching the detector from all ambient temperature components. The other curves, listed in the legend, show the totals with the slit assembly held constant at different temperatures, some cooled below ambient, and the rest of the components floating at the ambient temperature. We see that even with the slit cooled to -20 °C, sky-limited observations at R=7000 and λ = 1.7 μm would only be possible at the minimum winter temperatures. With the slit cooled to -40 °C these observations could be possible for T_{amb} < +10 °C, still excluding the summer months. Cooling the slit even more would make no

Figure 19. Total instrument backgrounds from the long slit and the ambient temperature optics with the slit cooled to different temperatures for a long wavelength cutoff of 1.7 μm.

Figure 21. Total thermal background from the long slit and the ambient temperature components with a slit emissivity range of 0.02-0.1, shown by the shaded regions, for a long wavelength cutoff of 1.7 μm.

difference because the limiting factor then becomes the ambient temperature optics. At that point the collimator and field lens would need to be actively cooled to improve performance.

We should note that **Figure 19** assumes the best conditions where the emissivity of the slit is assumed to be ε = 0.02, the value for a gold mirror. In reality, the slit coating will likely have a higher emissivity, increasing the slit

radiation by a factor of 3-5 (for ε = 0.06-0.1). If the slit emissivity is increased, the totals would change as shown by the shaded regions in **Figure 21**. A slit emissivity of 0.1 would preclude sky-limited observations at R ≥ 4000 with the slit cooled to -20 °C, requiring further cooling to -40 °C for operation at T_{amb} < +10 °C.

Figure 20. Total instrument backgrounds from the long slit and the ambient temperature optics as a function of slit temperature below ambient, dT_{slit}.

Even though the cooled slit would be purged with dry gas, local relative humidity and due points may limit how far below ambient temperatures we can practically cool the slit without creating condensation. Therefore, it is useful to replot the previous data as a function of slit temperature below ambient, dT_{slit}, rather than as absolute slit temperatures. This is

27

done in **Figure 20** for λ_{cutoff} = 1.7 μm. Preliminary analysis of the SALT relative humidity and due point data suggests that dT_{slit} = -20 to -30 ^{o}C should be possible to achieve, while minimizing condensation, under most conditions.

6.5.3   Ambient Temperature Optics

The next highest contribution of thermal background from **Figure 17** comes from the ambient temperature optics. The breakdown of thermal emission from the optical components is shown in **Table 11**, given as a percentage of the total background on the detector from the optics. The direction of the thermal emission from the element is given in the second column. Radiation initially headed toward the detector goes directly there through the optical system. Radiation initially headed toward the slit reflects off of it and then directly into the beam. The highest contribution comes from the flattest optics, for which the thermal radiation is emitted most directly into the beam along the optical axis.

Table 11. Breakdown of the thermal background at the detector from the optical elements.

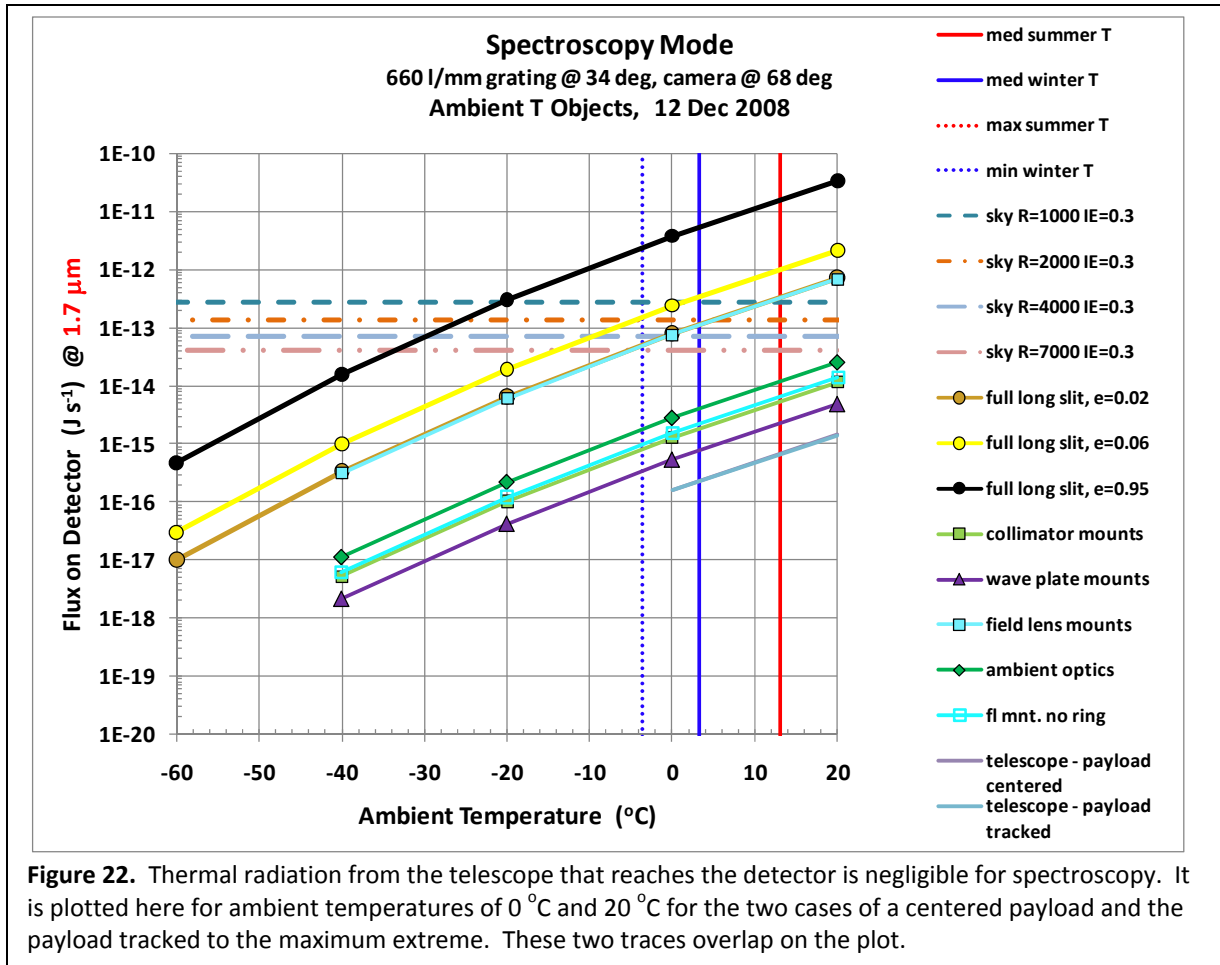| Element	Emission Direction	Percentage
NIR doublet	slit	24.04
waveplate compensator	detector	23.50
waveplate compensator	slit	14.55
collimator L3	detector	12.45
collimator L3	slit	7.87
collimator L2	detector	7.07
field lens 1	slit	3.58
collimator L2	slit	3.23
dichroic	detector	1.26
field lens 2	detector	1.17
dichroic	slit	0.71
collimator triplet 1	slit	0.36
collimator triplet 3	detector	0.22

A similar breakdown of the thermal radiation from components in the collimator lens mounts is given in **Table 12**. The highest contributor is the top ring facing the detector and the second highest is the bottom ring facing the slit. Both of these could be reduced if necessary by adding low emissivity angled radiation shields to the mount.

Table 12. Breakdown of the thermal background at the detector from the collimator mounts.

Source	Component	Percent
1	BLADDER_COVER_1_surface1_Face11	65.46
27	CELL_2_SEAT_1_surface1_Face3	33.35
18	ELEMENT_4_RETAINING_RING_2_1_surface1_Face4	0.42
17	ELEMENT_4_RETAINING_RING_2_1_surface1_Face1	0.37
5	ELEMENT_7_RETAINING_RING_1_surface1_Face4	0.31
25	CELL_2_SEAT_1_surface1_Face5	0.08

6.5.4 Telescope

Thermal emission from the telescope is not a problem for spectroscopy because the slit block most of the radiation. **Figure 22** shows the thermal background from the telescope that reaches the detector.

Figure 22. Thermal radiation from the telescope that reaches the detector is negligible for spectroscopy. It is plotted here for ambient temperatures of 0 °C and 20 °C for the two cases of a centered payload and the payload tracked to the maximum extreme. These two traces overlap on the plot.

6.5.5 Shorter Cutoff Wavelengths

Because the environmental conditions under which sky-limited spectroscopy out to λ = 1.7 μm at high spectral resolution will be very limited, we now explore the instrument background for shorter cutoff wavelengths. **Figure 23** shows the total thermal background due to the long slit and the ambient temperature components for λ_{cut} = 1.65, 1.6, 1.55, and 1.5 μm. For λ_{cut} = 1.6 μm (top right) we see that performance with no slit cooling, dT_{slit} = 0 °C, is nearly equal to that with dT_{slit} = -30 °C at λ_{cut} = 1.7 μm (**Figure 20**). With no slit cooling, λ_{cut} = 1.55 μm would allow sky-limited observations at the highest spectral resolutions up to the median summer temperature. With the slit cooled to dT_{slit} = -20 °C, the cutoff wavelength could be pushed out to λ_{cut} = 1.65 μm for the same performance. With the slit cooled to dT_{slit} = -30 °C, λ_{cut} = 1.7 μm observations at R=4000 would be close to the sky limit at the summer median temperature.

6.5.6 Environmental Conditions at SALT and Implications on Operability

Previously we analyzed the expected RSS-NIR thermal backgrounds at various temperatures. In this section we investigate SALT historical environmental data to translate the predicted instrument performance into operability on the telescope throughout the year. Average night time temperatures and distributions for the SALT site are shown in **Figure 24**. The top plot shows monthly night time averages over the period of Jan 2007 – Feb 2008. The lower two plots show temperature distributions for the hours between 18° astronomical twilight over the same time period.

Combining these data with our previous instrument background predictions, we now derive the percentages of astronomical hours during which sky-limited grating spectroscopy could be successfully obtained for our range of spectral resolutions. These percentages are shown in **Figure 25** for different long wavelength cutoffs as a function of the amount of slit cooling below the ambient temperature. The top left plot shows that for observations out to λ_{cutoff} = 1.7 μm with no slit cooling, sky-limited observations will never be possible, even at the lowest spectral resolution. Cooling the slit to 20 °C below ambient brings the available hours up to 19% of the time for R=7000, 47% for R=4000, and 74% for R=7000. Cooling the slit even more to 30 °C below ambient gives a vast improvement: 41% for R=7000, 69% for R=4000, and 97% for R=2000.
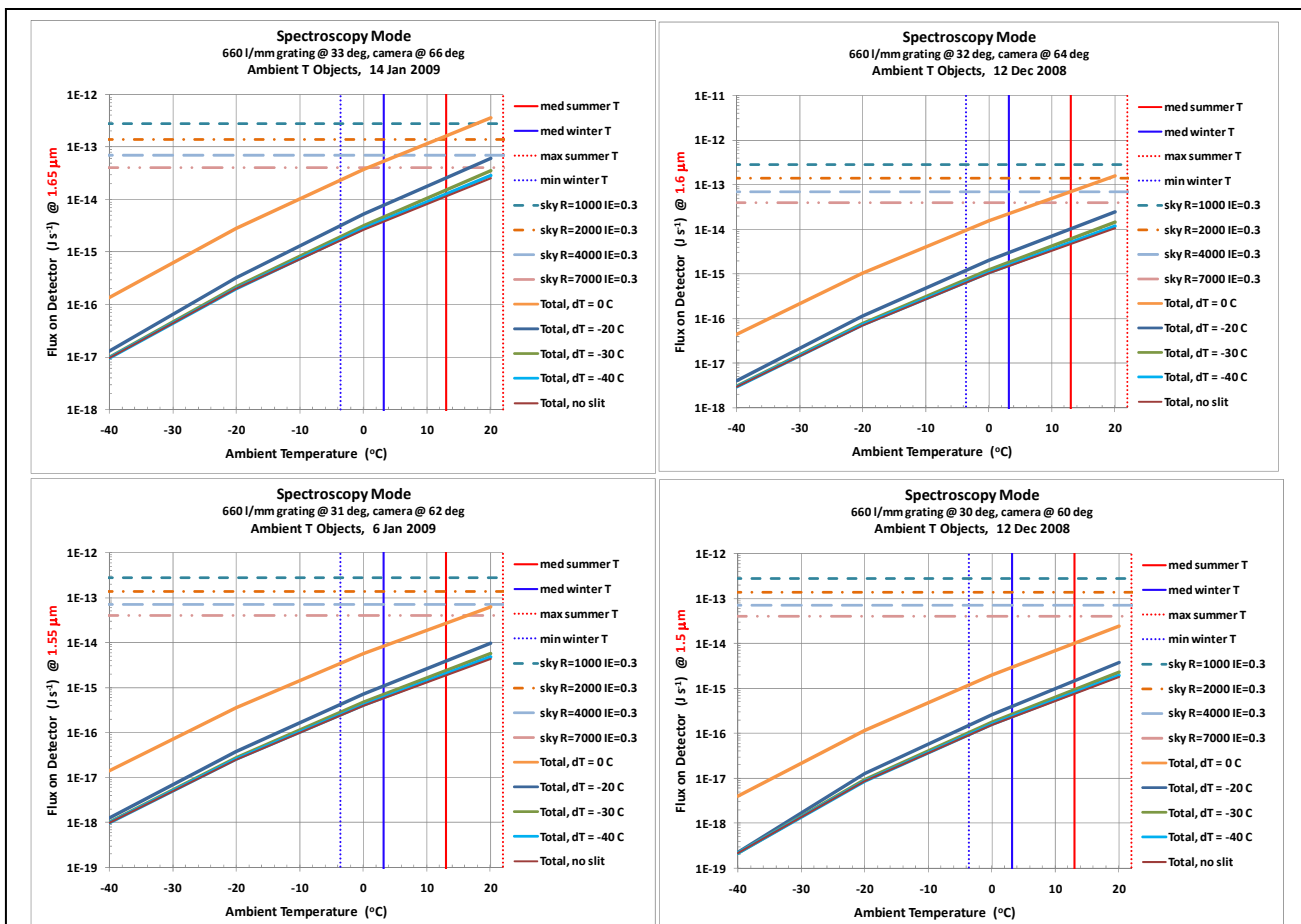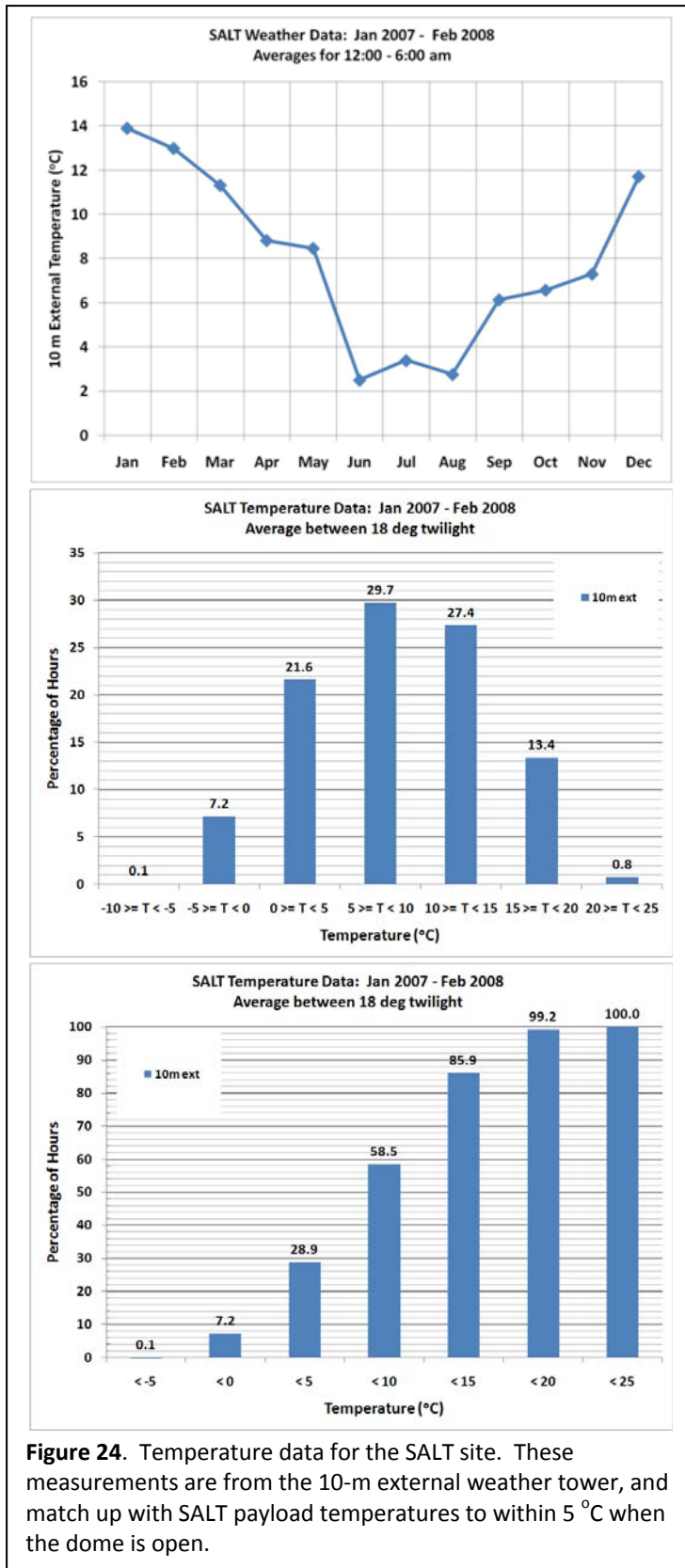

Figure 23. Total thermal background from the long slit and the ambient temperature components for long wavelength cutoffs of 1.65 μm (top left), 1.6 μm (top right), 1.55 μm (bottom left), and 1.5 μm (bottom right).
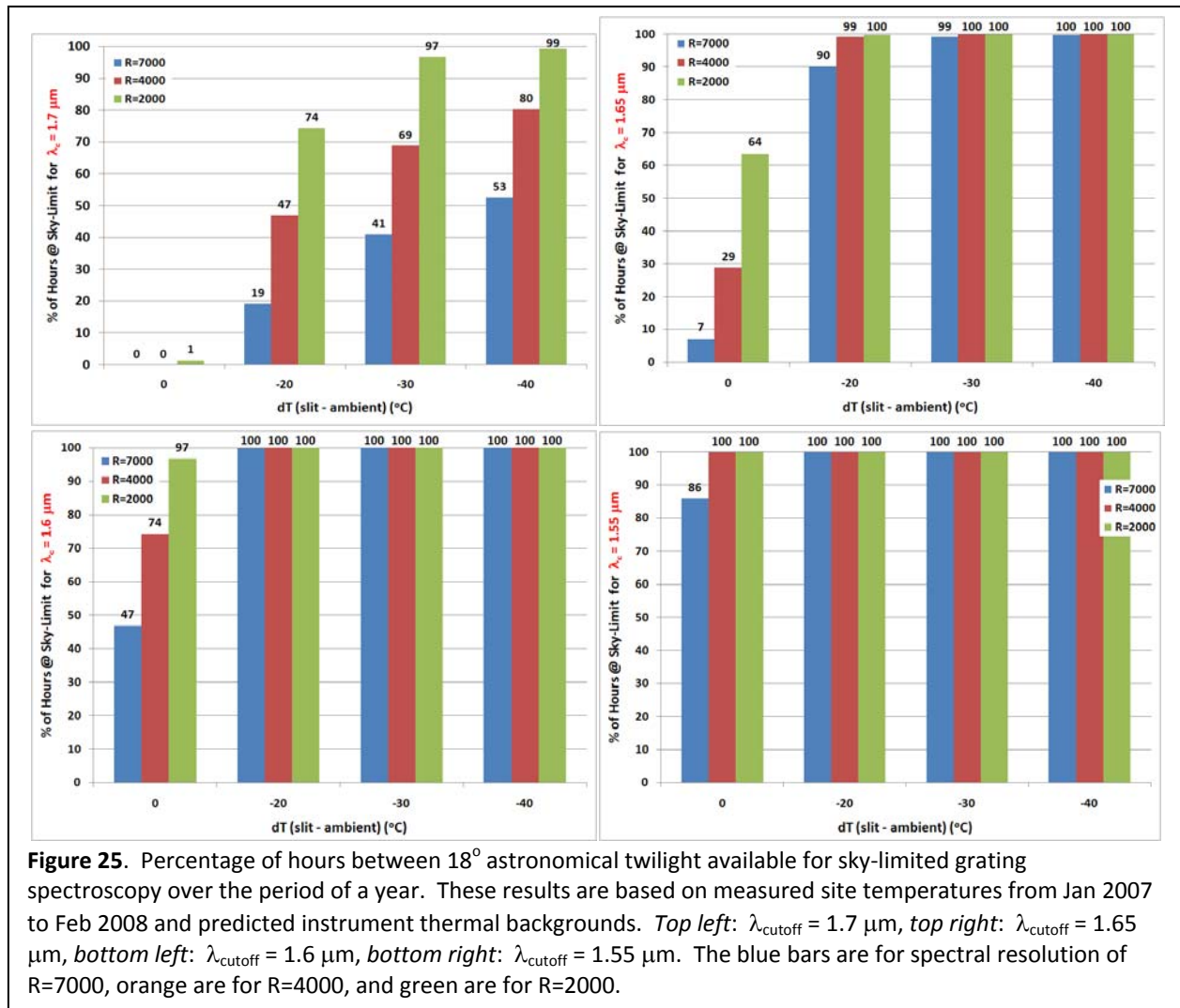
Figure 24. Temperature data for the SALT site. These measurements are from the 10-m external weather tower, and match up with SALT payload temperatures to within 5 °C when the dome is open.

An alternative to cooling the slit is to limit observations to a shorter cutoff wavelength. If the slit is not cooled at all, λ_{cutoff} = 1.6 μm (lower left plot) would allow sky-limited observations for comparable fractions of the time to the previous case of dT_{slit} = -30 °C out to λ = 1.7 μm: 47% at R=7000, 74% at R=4000, and 97% at R=2000. Cooling the slit to 40 °C below ambient does not gain much over 30 °C, and is not worth considering.

Table 13 summarizes the results for all cases analyzed using measured temperatures during astronomical twilight hours from Jan 2007 to Feb 2008 and predicted instrument thermal backgrounds for these temperatures. Column (1) is the assumed long wavelength cutoff (μm), column (2) is the amount of slit cooling below the ambient temperature (°C), column (3) is the ambient temperature (°C) below which sky-limited observations are possible for R=7000, column (4) is the number of hours for which this occurs, column (5) is the percentage of hours for which this occurs, column (6) is the ambient temperature (°C) below which sky-limited observations are possible for R=4000, column (7) is the number of hours for which this occurs, column (8) is the percentage of hours for which this occurs, column (9) is the ambient temperature (°C) below which sky-limited observations are possible for R=2000, column (10) is the number of hours for which this occurs, and column (11) is the percentage of hours for which this occurs.

Table 13. Hours available for sky-limited spectroscopy with RSS-NIR at SALT over the period of a year.

(1)	(2)	(3)	(4)	(5)	(6)	(7)	(8)	(9)	(10)	(11)
		R=7000			**R=4000**			**R=2000**		
λ_{cutoff}	dT_{slit}	T_{amb}	# hrs	% hrs	T_{amb}	# hrs	% hrs	T_{amb}	# hrs	% hrs
1.7	0	-12	0	0.0	-8	0	0.0	-2.5	48	1.4
1.7	-20	3	666	19.2	8	1627	46.9	13	2577	74.4
1.7	-30	7	1417	40.9	12	2385	68.8	18	3353	96.7
1.7	-40	9	1822	52.6	14	2784	80.3	20	3440	99.2
1.65	0	0	251	7.2	5	1000	28.9	11	2205	63.6
1.65	-20	16	3122	90.1	20	3440	99.2	22	3460	99.8
1.65	-30	20	3440	99.2	> 24	3466	100.0	> 24	3466	100.0
1.65	-40	> 22	3460	99.8	> 24	3466	100.0	> 24	3466	100.0
1.6	0	8	1627	46.9	13	2577	74.4	18	3353	96.7
1.6	-20	22	3460	99.8	> 22	3466	100.0	> 22	3466	100.0
1.6	-30	> 22	3466	100.0	> 22	3466	100.0	> 22	3466	100.0
1.6	-40	> 22	3466	100.0	> 22	3466	100.0	> 22	3466	100.0
1.55	0	15	2977	85.9	> 23	3464	99.9	> 23	3464	99.9
1.55	-20	> 24	3466	100.0	> 24	3466	100.0	> 24	3466	100.0
1.55	-30	> 24	3466	100.0	> 24	3466	100.0	> 24	3466	100.0
1.55	-40	> 24	3466	100.0	> 24	3466	100.0	> 24	3466	100.0
1.5	0	> 22	3460	99.8	> 23	3464	99.9	> 23	3464	99.9
1.5	-20	> 24	3466	100.0	> 24	3466	100.0	> 24	3466	100.0
1.5	-30	> 24	3466	100.0	> 24	3466	100.0	> 24	3466	100.0
1.5	-40	> 24	3466	100.0	> 24	3466	100.0	> 24	3466	100.0

Figure 25. Percentage of hours between 18° astronomical twilight available for sky-limited grating spectroscopy over the period of a year. These results are based on measured site temperatures from Jan 2007 to Feb 2008 and predicted instrument thermal backgrounds. *Top left*: λ_{cutoff} = 1.7 μm, *top right*: λ_{cutoff} = 1.65 μm, *bottom left*: λ_{cutoff} = 1.6 μm, *bottom right*: λ_{cutoff} = 1.55 μm. The blue bars are for spectral resolution of R=7000, orange are for R=4000, and green are for R=2000.

7   Long Wavelength Cutoff

7.1   Detector Quantum Efficiency Falloff

Little data exist on the falloff of detector quantum efficiency (QE) much beyond the cutoff wavelength. **Figure 26** shows a theoretical prediction from Teledyne (top). They claim that the detector sensitivity falls to a negligible level by 10% beyond the cutoff wavelength, which would be at λ = 1.87 μm for a λ_c = 1.7 μm cutoff detector. The two lower plots show a fit to the QE decrease of a HAWAII-2RG-1.7μm detector from the SNAP program (Schubnell et al. 2008, Ferlet 2008). When these data were measured, the SNAP test setup could only measure an absolute QE to 3-4% accuracy. Therefore, the data points only went to λ = 1.76 μm (Schubnell, private communication). This fit was extrapolated to longer wavelengths by Ferlet when analyzing thermal stray light for the FMOS fiber-fed NIR spectrographs on Subaru. The measured data show that the QE for this particular detector was down to 0.03 at λ = 1.76 μm. Assuming that the fit extrapolation holds, it predicts that the detector QE will be down to 2.46E-04 by λ = 1.87 μm, the Teledyne theoretical prediction of the point where sensitivity should be negligible.
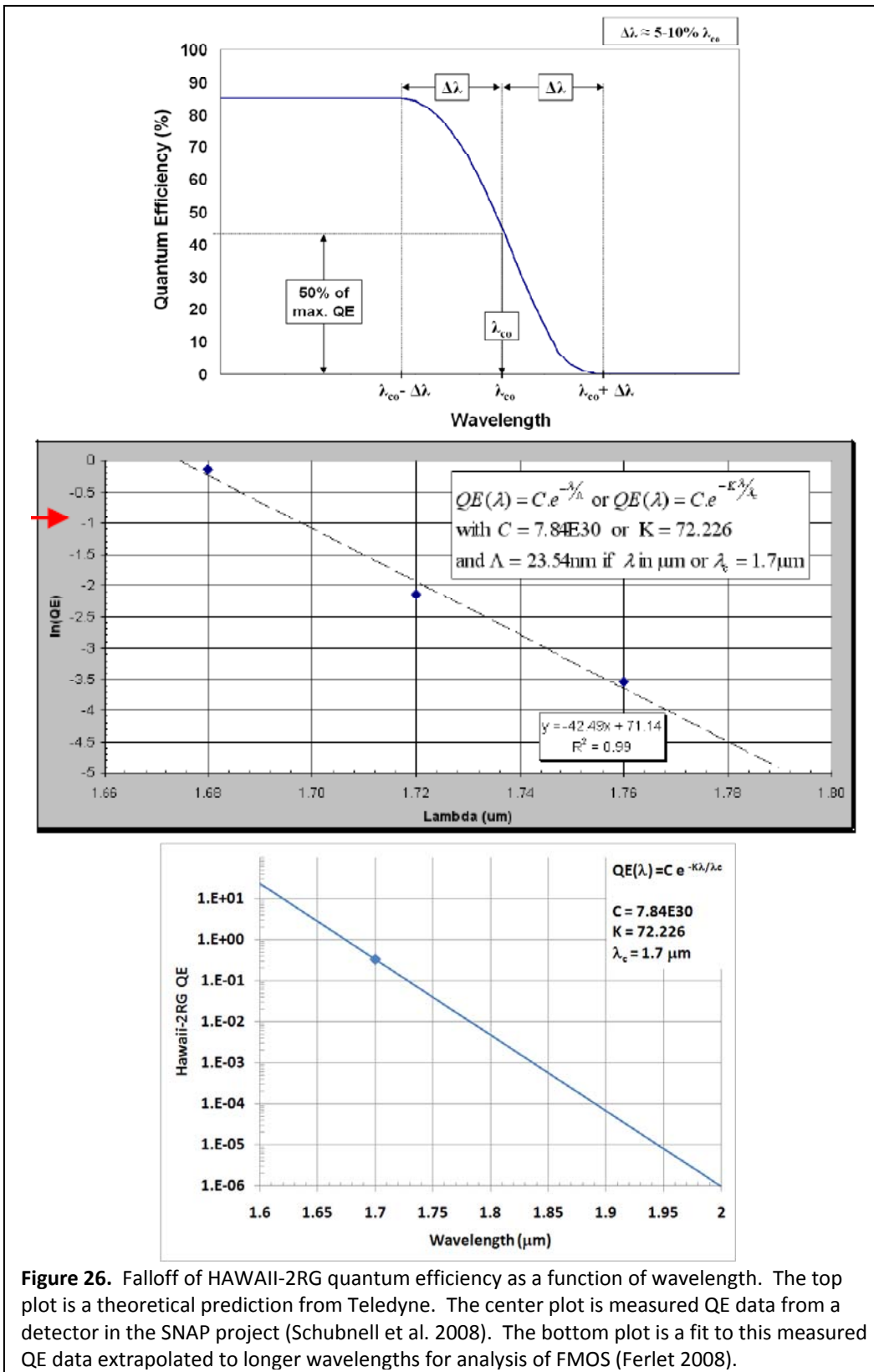
Figure 26. Falloff of HAWAII-2RG quantum efficiency as a function of wavelength. The top plot is a theoretical prediction from Teledyne. The center plot is measured QE data from a detector in the SNAP project (Schubnell et al. 2008). The bottom plot is a fit to this measured QE data extrapolated to longer wavelengths for analysis of FMOS (Ferlet 2008).

Once we find out our exact detector cutoff wavelength, based on the upcoming Teledyne manufacturing runs and their results, these existing detector QE data will be used to develop the final specifications for our long wavelength cutoff filter performance requirements.

7.2 Long Wavelength Blocking Filters

We have a 5 position filter wheel in the cryogenic dewar. One position will be open (or contain a filter that begins blocking at a wavelength beyond our detector cutoff to allow narrow band Fabry-Perot observations to go out as far as possible), one position is blocked off for detector calibrations, and 3 positions are for long wavelength cutoff filters. Based on the estimated instrument thermal backgrounds and the temperature statistics for the SALT site, we can pick long wavelength cutoffs that will allow sky-limited spectroscopy to be carried out in different ambient conditions. **Figure 25** gives the typical percentages of astronomically dark hours available for sky-limited spectroscopic observations over the course of a year. We are currently baselining no slit cooling, with it left as a future upgrade path. This means that the filters we choose now should assume no slit cooling.

We have initially chosen cutoff wavelengths of λ_{cutoff} = 1.65-1.67 μm, 1.6 μm, and 1.55 μm for our 3 blocking filters. The longest range is to allow observations of the Fe II 1.644 μm line, desired by many science programs. Thermal modeling to date has shown that with a cutoff at 1.65 μm, sky-limited spectroscopy could be done 29% of the time at R=4000 and 7% of the time at R=7000. Further modeling will determine just how far beyond 1.65 μm we can push so that observations of the 1.644 μm line will not be compromised and we will still have acceptable thermal background levels. The 1.6 and 1.55 μm cutoffs will be selectable based on nightly ambient temperatures and what observations are in the SALT queue. At 1.55 μm, sky-limited spectroscopy at R=7000 should be possible 86% of the time. Shortening this wavelength any would quickly get into the atmospheric absorption trough at 1.35-1.45 μm, making the extra ~0.5 μm hardly worth the incremental extra coverage. After further detailed thermal analyses and science case development, the exact wavelengths of these 3 cutoff filters can be modified before the critical design stage with no impact to the instrument design.

8 Similar Instruments

A number of NIR instruments have attempted designs that were not fully cryogenic and relied on long wavelength blocking filters. Some were successful and some were not, where the level of success seems to depend heavily on the correct implementation of blocking filters.

CIRPASS (Parry et al. 2004) was a very successful fiber-fed NIR spectrograph used as a visiting instrument on Gemini and on the William Herschel Telescope. It operates at a spectral resolution of R~3000 out to wavelengths of 1.67 or 1.8 μm. The spectrograph resides inside a freezer operating at -40 $^{\circ}$C. Long wavelength blocking filters are contained within the cryogenic dewar. One with a cutoff at 1.85 μm stays permanently mounted in the beam, and additional filters with cutoffs at 1.4 and 1.67 μm are selectable via a filter wheel.

FMOS (Dalton et al. 2006) is a fiber-fed spectrograph currently being commissioned on Subaru. Its design is partly based on CIRPASS. The spectrograph resides in a -70 ^{o}C freezer. The detector is sensitive out to λ = 2.5 μm, but light beyond 1.8 μm is blocked with a single cutoff filter. Initial commissioning revealed that the cutoff filter had not been properly specified for blocking far enough beyond the 2.5 μm detector cutoff. A filter leak at ~2.7 μm led to a large thermal background reaching the detector. The cutoff filter was corrected, and now instrument thermal backgrounds match very closely the levels predicted by their thermal modeling using ASAP (Gavin Dalton, private communication).

LRS-J (Tufts et al. 2004) was an extension to the Low Resolution Spectrograph (LRS) on the Hobby-Eberly Telescope (HET). It suffered from similar thermal background problems as FMOS. It used a 2.5 μm sensitive detector with a cutoff filter blocking λ > 1.35 μm because no instrument cooling was implemented upstream of the cryogenic dewar containing the blocking filter, camera optics, and detector. The thermal background difference at λ = 1.35 and 2.5 μm is 7 orders of magnitude – too much blocking to get from a single filter.

All of these instruments used a detector that was sensitive out to λ = 2.5 μm. We believe that our selection of a detector cutoff wavelength of 1.7 μm will be a large step in the right direction of making our implementation a success. Our required blocking level at 1.7 μm will be 5 orders of magnitude below the background at λ = 2.5 μm. This fact, coupled with our extensive thermal analysis and ray tracing, and the fact that we have planned a number of cutoff filters that can be used in different ambient operating conditions, should all work together to make RSS-NIR a success.

9   Summary and Conclusions

Pre-dewar operating at -40 ^{o}C. Our initial thermal analysis of RSS-NIR used a conceptual instrument design, with existing components common to RSS-VIS, to estimate the required operating temperature of the pre-dewar. This was important early in the project as part of the instrument feasibility study. We determined that with an operating temperature of -40 ^{o}C, the thermal emission from the pre-dewar and its components will be negligible. The total background from the pre-dewar components will be a factor of ~5 below the lowest ambient temperature component and a factor of ~20 below the sky for spectroscopy at R=7000. This temperature is also good from the practical standpoint that a number of commercial mechanisms are rated for operation down to this temperature.

Slit cooling. We performed an analysis of the effects of cooling the slit. Thermal emission from this component is the largest contributor to the instrument's thermal background. We determined that cooling the slit to 30 ^{o}C below ambient would significantly increase the operability of RSS-NIR for sky-limited spectroscopy on faint targets (Section 6.5.6). An engineering feasibility study identified viable methods for implementing the cooling. However, at this time slit cooling is left as a future upgrade path (due to budgetary reasons) and not included in the baseline instrument design. For sky-limited spectroscopy, an ambient temperature slit will limit our long wavelength cutoff to λ ~ 1.65 μm, achievable in typical annual conditions 7% of the time at R=7000 and 29% of the time at R=4000.

Gold-coating the slits. All thermal analyses have assumed low emissivity gold coated slits. This is essential for operation beyond the J-band. Gold coating is relatively straightforward for the long slits. We are currently investigating methods for gold coating the carbon fiber multi-object spectroscopy slit masks. Since the slits in these masks are custom cut with a laser at the SALT facility, we will have to develop a process for doing so on gold-coated mask substrates. Carbon fiber mask blanks are currently being gold coated by 2 different companies and laser cutting tests at the SALT facility will follow. Our initial plan is to develop a process by which pre-coated blanks are supplied to SALT with either a durable enough coating to surviving slit cutting process, or with an overcoat that can be peeled off after slit cutting. (See the RSS-NIR Midterm Review Redbook for more details.)

Long wavelength cutoffs. Based on our thermal analyses, we have designed a 5-position cryogenic filter wheel inside the detector dewar. One position is open to allow observations out to the detector sensitivity cutoff, one is blanked off for detector calibrations, and three are for different long wavelength blocking filters. This will allow flexibility in sky-limited spectroscopic observations in varying ambient observatory temperatures. The longest wavelength will be at 1.65-1.67 µm. An [Fe II] feature at 1.644 µm is one desired by many science observations in the nearby ISM and star forming regions. Further thermal analysis will determine whether we can push this cutoff out far enough to not compromise this line, while still maintaining a reasonable instrument background. The other two cutoff wavelengths will be at λ = 1.6 and 1.55 µm. These will allow sky-limited spectroscopy to be conducted most of the time at SALT (Section 6.5.6). We will use all information available on our specific detector long wavelength quantum efficiency falloff to specify the performance requirements on our blocking filters.

Identification of problem components. Our ASAP analysis has already identified one component that would have contributed significant instrument thermal background. This was the retaining ring on the field lens mount in the common optical path. We have modified this component to bring its thermal emission down to a tolerable level. This was an unexpected result that would have prevented the instrument from meeting its performance specifications, and one that we would not have caught without the ASAP analysis. It is also a good example of the interactive design philosophy between thermal analysis and mechanical design that we have adopted for RSS-NIR.

10 Future Work

Now that the mechanical design is maturing, detailed pre-dewar thermal analyses with actual components will be conducted. In these analyses we will determine required operating temperatures of key components like the NIR collimator doublet. This doublet is the window into the pre-dewar and the second element is a CaF_2 lens, which is very sensitive to thermal gradients. We will analyze in ASAP the maximum allowable temperature for this element to keep its thermal background down, and minimize the induced thermal stresses to this element in the mechanical mount and cooling designs. Other components, such as the articulation rail and pivot hub, penetrate through the pre-dewar floor. These components may not reach the nominal pre-dewar temperature, so ASAP analyses will determine where we require radiation shields to protect the detector from the radiation from such components. We will

design all radiation shielding, baffling, and the cold pupil mask within the pre-dewar by iterating between ASAP thermal analyses and detailed mechanical designs.

To date, only spectroscopic modes of RSS-NIR have been thermally analyzed. The next steps will include the Fabry-Perot instrument modes. We expect to be able to observe out to the detector cutoff with these modes, since only a narrow spectral band is transmitted by the etalon. Nevertheless, this will be thoroughly analyzed in ASAP, including the effects of the large etalon lineshape wings in the presence of bright night sky emission lines.

Finally, we will perform a detailed ghost analysis of the instrument in ASAP. This will include all thermal scattered light, as well as a VPHG ghost analysis as was done for FMOS (Ferlet 2008).

11 References

Dalton, G.B., Lewis, I.J., Bonfield, D.G., Holmes, A.R., Brooks, C.B., Lee, H., Tosh, I.A.J., Froud, T.R., Patel, M., Dipper, N.A., Blackburn, C., 2006, Proc. SPIE, 6269, 62694A-1.

Ferlet, M.J., 2008, Proc. SPIE, 7014, 701436.

Parry, I., Bunker, A., Dean, A, Doherty, M., Horton, A., King, D., Lemoine-Busserole, M., Mackay, C., McMahon, R., edlen, S., harp, R., Smith, J., 2004, Proc. SPIE, 5492, 1135.

M. Schubnell, M., Brown, M. G., Karabina, A., Lorenzon, W, Mostek, N., Mufson, S.,. Tarlé, G, Weaverdyck, C., 2008, Proc. SPIE 7021, 70210L.

Tufts, J.R., Hill, G.J., MacQueen, P.J., Wolf, M.J., 2004, Proc. SPIE, 5492, 1150.